

RICE UNIVERSITY

Magneto-Optical Spectroscopy of Metallic Carbon Nanotubes

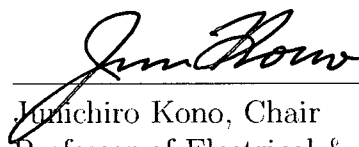
by

Thomas A. Searles, Jr.

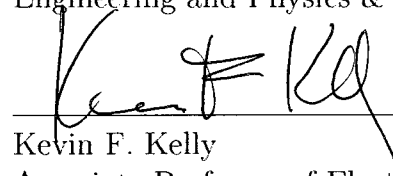
A THESIS SUBMITTED
IN PARTIAL FULFILLMENT OF THE
REQUIREMENTS FOR THE DEGREE

Masters of Science

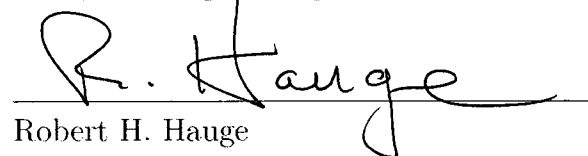
APPROVED, THESIS COMMITTEE:



Junichiro Kono, Chair
Professor of Electrical & Computer
Engineering and Physics & Astronomy



Kevin F. Kelly
Associate Professor of Electrical &
Computer Engineering



Robert H. Hauge
Distinguished Faculty Fellow in
Chemistry

Houston, Texas

August, 2009

UMI Number: 1485970

All rights reserved

INFORMATION TO ALL USERS

The quality of this reproduction is dependent upon the quality of the copy submitted.

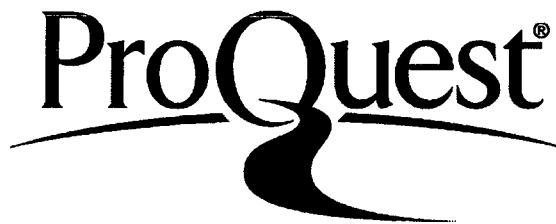
In the unlikely event that the author did not send a complete manuscript and there are missing pages, these will be noted. Also, if material had to be removed, a note will indicate the deletion.



UMI 1485970

Copyright 2010 by ProQuest LLC.

All rights reserved. This edition of the work is protected against unauthorized copying under Title 17, United States Code.



ProQuest LLC
789 East Eisenhower Parkway
P.O. Box 1346
Ann Arbor, MI 48106-1346

ABSTRACT

Magneto-Optical Spectroscopy of Metallic Carbon Nanotubes

by

Thomas A. Searles, Jr.

Through polarization-dependent magneto-optical absorption spectroscopy, the magnetic susceptibility anisotropy for metallic single-walled carbon nanotubes has been extracted and found to be up to $4\times$ greater than values for semiconducting single-walled carbon nanotubes. Consistent with theoretical predictions, this is the first experimental evidence of the paramagnetic nature arising from the Aharonov-Bohm-phase-induced gap opening in metallic nanotubes. We also compare our values with previous work for semiconducting nanotubes, which confirm a break from the prediction that the magnetic susceptibility anisotropy increases linearly with the diameter.

Acknowledgements

I would first like to thank my Lord and savior Jesus Christ for giving me strength and guidance; and most importantly for ordering my steps in this journey called graduate school. Also a very special thanks to my family for being very loving and understanding during this work.

The National Society of Black Physicists and my professors at Morehouse College showed me very early in my career that great science is done everyday by those that look like me and I am forever indebted to both organizations for their influence.

Thank you to Dr. Kono for affording me the opportunity to travel to Japan and complete the present work. Also for the knowledge that I've gained as his student. Also, thanks to my committee for their patience and coming together at the last minute to advance my education.

For all of my colleagues and friends that I've met in graduate school thank you very much for allowing me to keep my personality and for serving as a resource for borrowing things for my experiment and support for when experiments don't work.

Thanks to my funding agencies, especially the Office of Naval Research who has allowed me a freedom that only other Fellows know is possible. Also to Ms. Theresa L. Chatman for being my "auntie" in Houston and running the very busy AGEP office.

To my collaborators on this project and the many others that were not as successful, thank you for your patience and knowledge that I've gained along the way learning from you at various magnet labs around the world. I'd also like to thank Dr. Lee Johnson of NRL for the best summer intern experience of my life.

To April and Sadie, I know that I was away a lot and I am very appreciative of allowing me a life to come back to that is both full of love, happiness, and at many times rest and relaxation.

Contents

Abstract	ii
List of Illustrations	iv
List of Tables	v
1 Magnetic Properties of Graphitic Materials	1
2 Theory for Magnetic Properties of SWNTs	6
2.1 Single-Walled Carbon Nanotubes	6
2.2 Aharonov-Bohm Effect on Optical Absorption of SWNTs	7
2.3 Novel Magnetic Properties of SWNTs	8
3 Previous Work on Magnetic Susceptibility Anisotropy of Semiconducting Nanotubes	16
3.1 Estimation of $\Delta\chi$ using Magneto-Photoluminescence	16
3.2 Measurement of the Polarized Optical Absorption Cross Section of SWNTs	17
3.3 Influence of Ferromagnetic Particles on $\Delta\chi$	19
3.4 Chirality Dependence of $\Delta\chi$	22
4 Magnetic Susceptibility Anisotropy of Metallic SWNTs	24
4.1 Experimental Methods	24
4.1.1 Sample	24
4.1.2 Hybrid Magnet	28
4.1.3 Experimental Setup	29

4.2	Experimental results	29
4.3	Analysis	36
4.3.1	Fitting Methods	36
4.3.2	Fitting Results	39
4.4	Discussion	43
4.5	Conclusion	48
	Bibliography	49

Illustrations

1.1	Graphene is the starting material for many carbon allotropes including all carbon nanomaterials. Each have their own unique physical properties depending on structure/chirality, size, and dimensionality. The 0D buckyball (left) is shown along with the 1D single-walled carbon nanotube (middle) and graphene sheets/graphite (right); adapted from [5].	3
1.2	Magnetic susceptibilities as a function of temperature of various carbon derivatives where CGS ppm/mol = emu $\times 10^{-6}$ /mol. Adapted from [1, 11]	4
2.1	Graphene sheet with labeled (n, m) for metallic and semiconducting SWNTs from Ref. [15].	10
2.2	Dispersion E vs. k for semiconducting (6,5) nanotube. (Developed through the use of the nanotube calculator (Boston University)) . . .	11
2.3	Dispersion E vs. k for metallic (6,6) nanotube. (Developed through the use of the nanotube calculator (Boston University))	12
2.4	Bandgap as a function of magnetic flux through the nanotube. Note that it oscillates for both semiconducting ($\nu = \pm 1$) and metallic ($\nu = 0$) nanotubes. (Ref. [17]))	13

2.5	(a) Bandgap as a function of Fermi Energy, E_f . (b) χ_{\perp} for semiconducting ($\nu = \pm 1$) and metallic nanotubes ($\nu = 0$) as a function of E_f (c) χ_{\parallel} for semiconducting and metallic nanotubes as a function of E_f (Ref. [23]).	14
2.6	Angular dependence of χ for SWNTs, where $\theta = 90^\circ$ is χ_{\perp} and $\theta = 0^\circ$ is χ_{\parallel} . Note that $\Delta\chi$ for metallic nanotubes (dotted) is 5 larger than $\Delta\chi$ for semiconducting nanotubes (dashed) (Ref. [24]).	15
3.1	Magneto-PL spectra of HiPco SWNTs up to 45T from Ref [25]. Note that for all chiralities present, there is a substantial redshift for each peak. The inset shows the diameter dependence of u as defined in ??	17
3.2	(a) Polarized optical absorption cross section data for semiconducting laser oven SWNTs f(b) Average of the spectra from the four samples (c) Modeling of spectra of (b) to show the effect of depolarization The solid curve is for σ_{\parallel} . And the dashed line is for σ_{\perp} with depolarization effect and the dotted is σ_{\perp} without this effect. Adapted from Ref. [26].	18
3.3	$S(B)$ for fractionated (no contribution from ferromagnetic (FM) particles) and unfractionated (with contribution) (a) HiPco and (b) laser oven SWNTs [27].	20
3.4	$S(B)$ for $\vec{\mu}$ -driven (SWNTs aligning due to FM particle contribution and magnetic susceptibility anisotropy denoted by the solid line) and $\Delta\chi$ -driven (alignment is only from magnetic susceptibility anisotropy denoted by the dashed line) SWNTs. Note that the latter has a much lore alignment, whereas the former reaches complete alignment at much smaller fields [27].	21
3.5	$\Delta\chi$ as a function for diameter for semiconducting CoMoCAT nanotubes from Ref [28]. The data in (a) is fit to the family dependent theory shown in B for many nanotubes.	23

4.1	PLE map of our NIST (6,5)-enriched length- sorted CoMoCAT sample. Note that there are only a few chiralities present. Also note that in the “Valley of the metals” there is no luminescence present.	25
4.2	Absorbance spectra from UV-Vis NIR Spectroscopy of our NIST (6,5)-enriched length- sorted CoMoCAT sample.	26
4.3	Resistive Magnet Insert Coils of Bitter Magnet adapted from [33]	30
4.4	Photograph of the NIMS Hybrid Magnet	31
4.5	Optical path of Polarized Magneto-optical Absorption Spectroscopy Probe [35].	32
4.6	Polarized Magneto-optical Absorption Spectroscopy from 0 to 35 T	34
4.7	Absorbance spectra (solid black) for 0 T and 35 T with all peaks assigned from our sample. The unpolarized isotropic absorbance (dashed red) is calculated from the magnetic field data and agrees well with that of the 0 T data.	35
4.8	Reduced Linear Dichroism vs Energy (eV) from measured data. The largest peak is from metallic nanotubes (6,6) and (7,4).	35
4.9	Fitting results for 0 T and 35 T. The data (black) is fit by the sum of each individual chirality nanotube (blue) and the addition of a susceptible offset (blue). The sum of these individual fits is shown as a red line. All spectra were fit simultaneously and data for subsequent fields was performed in the same manner.	38
4.10	Lorentzians for different chirality nanotubes at 0 and 35 T.	40
4.11	LD^r vs. Energy (eV) derived from fitting for each individual chirality nanotube in our sample. The metallic tubes (red) are higher than the semiconducting nanotubes (blue dotted).	41
4.12	S vs B	42
4.13	Model of S vs. u	44
4.14	S vs. B of (6,6) vs. (6,5)	46

Tables

1.1	Values of χ for Carbon Allotropes: All values are $\sim 10^{-6}$ emu/mol.	5
4.1	Comparison of values of magnetic susceptibility anisotropy from previous theoretical and experimental studies and this work. For each chirality nanotube (n,m), the diameter d and the chiral index ν is given followed by estimated theoretical and experimental values of $\Delta\chi$. All values for $\Delta\chi$ are $\sim 10^{-5}$ emu/mol with the first two columns of $\Delta\chi_{th}$ corresponding to theoretical predictions. For the last two columns, $\Delta\chi_{exp}$ are measured values for $\Delta\chi$ with the last column for the present work.	47

Chapter 1

Magnetic Properties of Graphitic Materials

The magnetic properties of the derivatives of carbon have been thoroughly researched and discussed over the past 80 years with a multitude of interest concerning the diamagnetic response of graphite[1]. The total magnetic susceptibility, χ , of graphite is reported to be -88×10^{-6} emu/mol at room temperature[1], more than ten times larger than that of diamond ($\chi(\text{diamond}) = -5.5 \times 10^{-6}$ emu/mol[1]). As a comparison, the only other materials with larger diamagnetism than graphite are superconductors which are perfectly diamagnetic, $\chi(\text{superconductor}) = -1$ emu/mol. One can even find many videos about the large diamagnetism of graphite on YouTube such as one featuring a toy based on the magnetic levitation created by small blocks of graphite [2] and another demonstrating a floating pencil lead [3].

Magnetic susceptibility is defined by the following [4]:

$$M \equiv \chi H \tag{1.1}$$

where M is the magnetization intrinsic to the material and H is the applied magnetic field. When $\chi > 0$, the material is said to be paramagnetic where the magnetic dipole moment of the system orients toward the direction of the applied magnetic field [4]. Conversely, when $\chi < 0$, the material is diamagnetic, and the magnetic dipole

moment repels from the applied magnetic field [4]. The third category of magnetism is ferromagnetism in which no applied magnetic field is necessary for magnetization to be present.

Conventional allotropes of carbon are diamond, graphite, and graphene. Advances in material science and nanotechnology have developed other carbon derivatives such as graphene oxide [6], graphene nanoribbons [7], fullerenes [8], and single-walled carbon nanotubes (SWNTs) [9, 10]. As the structure and size of these materials change, the physical properties can be vastly different [5].

As an example of how structure and size can play a part in determining differences in magnetic susceptibility, we can briefly introduce the “original” buckyball C_{60} and its close relative C_{70} . The magnetic susceptibility of C_{60} is given to be $\sim -4 \times 10^{-6}$ emu/mol [11], on the same order as $\chi(\text{diamond})$. However, $\chi(C_{60})$ is more than two times less than $\chi(C_{70})$ even though they are in the same family of allotropes [12]. Furthermore, C_{60} contains a benzene ring structure which many have attributed to the large diamagnetism seen at room temperature for graphite [1]. Table 1.1 details magnetic susceptibilities of graphitic materials as reported in the literature.

At room temperature as seen in Fig. 1.2, SWNTs, regardless of whether they are metallic or semiconducting, are predicted to behave like graphite, with the first estimation of diamagnetism for bundled nanotubes even greater than that of graphite. However, structure/chirality and magnetic field play an important role in determining the magnetic susceptibility anisotropy ($\Delta\chi = |\chi_{\parallel} - \chi_{\perp}|$) seen in individualized SWNTs

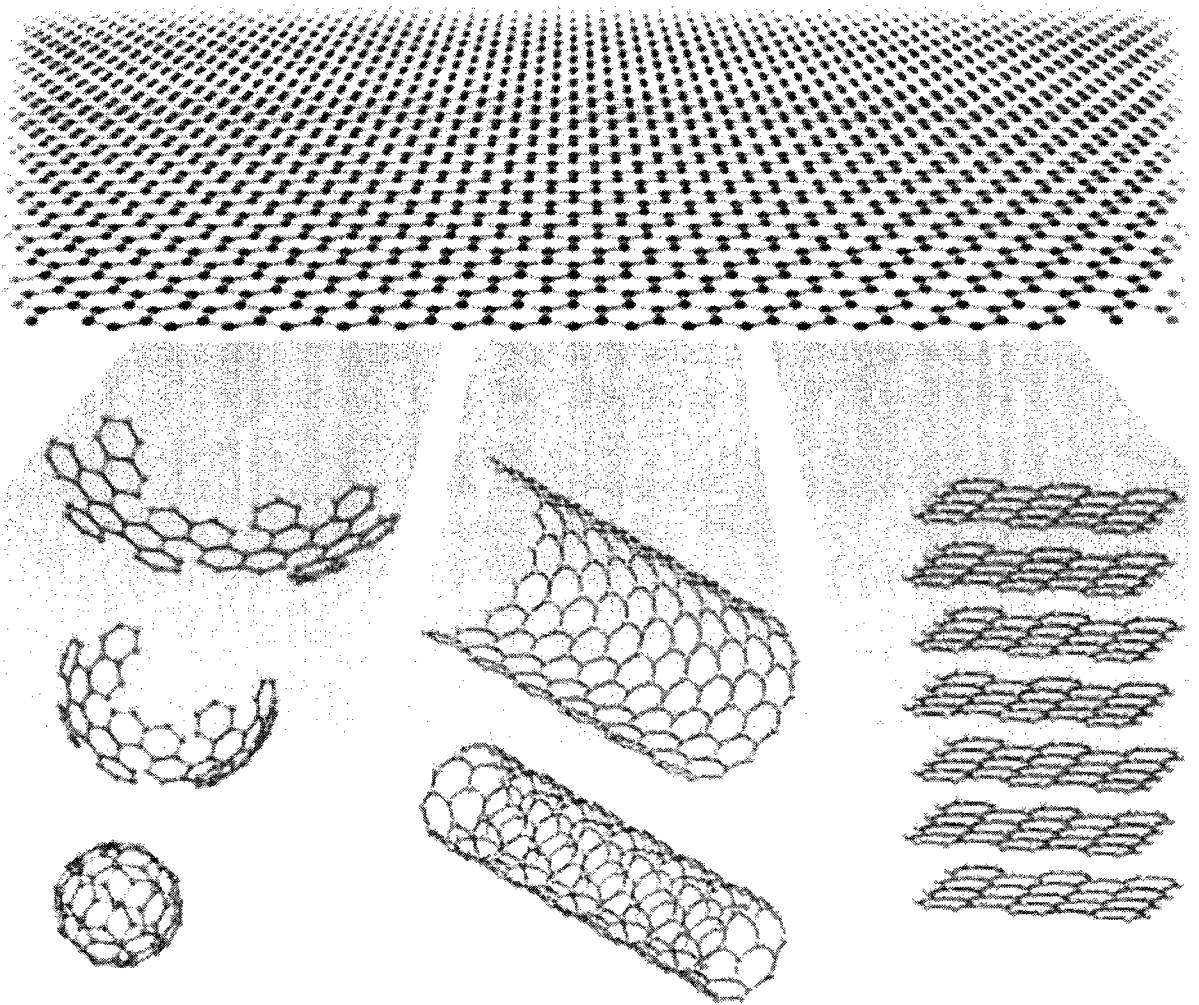


Figure 1.1 : Graphene is the starting material for many carbon allotropes including all carbon nanomaterials. Each have their own unique physical properties depending on structure/chirality, size, and dimensionality. The 0D buckyball (left) is shown along with the 1D single-walled carbon nanotube (middle) and graphene sheets/graphite (right); adapted from [5].

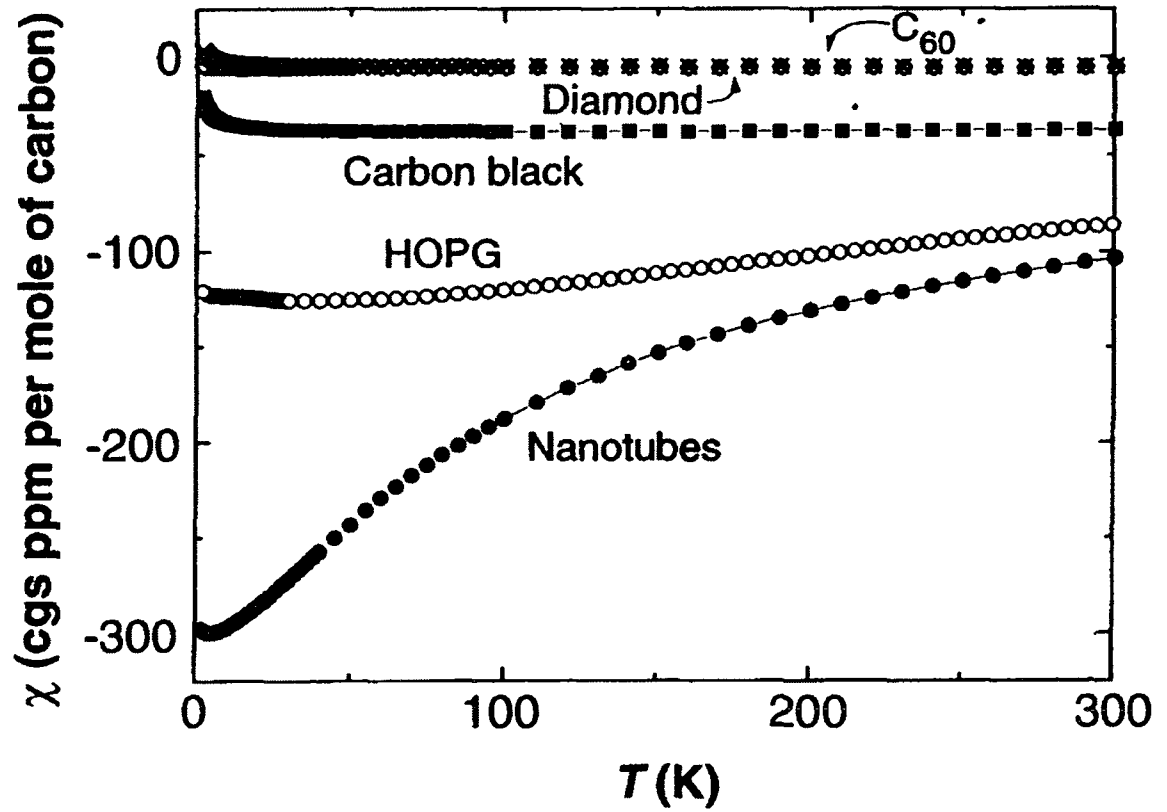


Figure 1.2 : Magnetic susceptibilities as a function of temperature of various carbon derivatives where CGS ppm/mol = emu $\times 10^{-6}$ /mol. Adapted from [1, 11]

Table 1.1 : Values of χ for Carbon Allotropes: All values are $\sim 10^{-6}$ emu/mol.

<i>Material</i>	χ
Graphite/HPGO[1]	-88
Bundled SWNTs[11]	-120
Diamond[1]	-5.5
C ₆₀ [11]	-4.23
C ₇₀ [12]	-7.1

where χ_{\parallel} is the magnetic susceptibility along the nanotube axis and χ_{\perp} is the magnetic susceptibility transverse to the nanotube axis.

Throughout this thesis, the focus will be on explaining and detailing our latest work on the magnetic properties of SWNTs. Specifically, it will determine the $\Delta\chi$ for metallic SWNTs which is theorized to be $2 - 5\times$ larger than $\Delta\chi$ for semiconducting nanotubes. First, in chapter 2, we will explain the theory behind the novel magnetic properties of SWNTs as a result of the Aharonov-Bohm physics [13, 14] at high magnetic fields. Then, in chapter 3, we will detail recent experimental work on the magnetic susceptibility anisotropy of semiconducting nanotubes. The heart of the thesis, chapter 4, will contain results from our magnetic linear dichroism experiment up to 35 T on CoMoCAT SWNTs in which we extracted the large predicted value of the magnetic susceptibility anisotropy and compared those values directly with semiconducting nanotubes in the same sample for the first time.

Chapter 2

Theory for Magnetic Properties of SWNTs

2.1 Single-Walled Carbon Nanotubes

Single-walled carbon nanotubes (SWNTs) are cylindrical sheets of graphene with diameter on the scale of ~ 1 nm. Depending on the chirality (the manner in which the graphene sheet is rolled), the physical properties of SWNTs change, making them an interesting system to study 1D physics. The chiral vector is defined as:

$$\vec{C}_h = n\vec{a}_1 + m\vec{a}_2 \quad (2.1)$$

where \vec{a}_1 and \vec{a}_2 are the unit vectors determined by the lattice constant a of graphene such that $a = |\vec{a}_1| = |\vec{a}_2| = 2.46$ Å. Each chiral index (n, m) represents a particular type of SWNT as seen in Fig. 2.1. There are three main types of nanotubes defined by (n, m) : chiral ($n \neq m, m \neq 0$), zigzag ($n, 0$), and armchair ($n = m$). From (n, m) , one can determine parameters such as the diameter, number of C atoms per unit cell, and the crystal structure. The band structure of nanotubes can be described by the linear dispersion of a graphene sheet under cylindrical boundary conditions:

$$E(|\vec{k}_{2D}|) = |\vec{k}_{2D}|\gamma_0 a \quad (2.2)$$

where $|\vec{k}_{2D}|$ is the 2D wave vector and γ_0 is the overlap integral.

Under these conditions, the electrons in this system move as planar Bloch wavefunctions described by:

$$\psi_{n\vec{k}}(\vec{r} + \vec{C}_h) = e^{i\vec{k}\vec{C}_h} \psi_{n\vec{k}}(\vec{r}) \quad (2.3)$$

\vec{C}_h can be viewed as a “cutting line” across the graphene lattice. If this vector passes through the K point of the 1st Brillouin Zone, the bandgap = 0 and the nanotube is metallic. When \vec{C}_h does not pass through the K point, then the nanotube is semiconducting. As a simple rule, a nanotube with index (n, m) is metallic if:

$$(n - m) \bmod 3 = 0. \quad (2.4)$$

Equation 2.4 is a result of the boundary conditions set on the wavefunction of a graphene sheet shaped into a cylinder. According to this simple rule, armchair nanotubes are always metallic. If (n, m) for other types of tubes do not satisfy this rule then the nanotube is semiconducting. The dispersions of the semiconducting (6,5) nanotube and the metallic (6,6) nanotube can be seen in Fig. 2.2 and Fig. 2.3.

2.2 Aharonov-Bohm Effect on Optical Absorption of SWNTs

Ajiki and Ando reported calculations showing that the band structure for SWNTs changes as a function of the amount of Aharonov-Bohm flux [13, 14] through the center of the nanotube [16].

Depending on the amount of flux, the bandgap oscillates between having semiconducting and metallic properties as seen in Fig. 2.2. Furthermore, metallic and semiconducting nanotubes respond to Aharonov-Bohm flux in opposite ways; i.e. the

band gap shrinks with magnetic field for semiconducting nanotubes and increases with magnetic field for metallic nanotubes. They predicted that through polarized optical absorption spectroscopy this theory could be realized due to the optical selection rules of SWNTs. Light polarized parallel to the tube axis is absorbed whereas light polarized perpendicular is not absorbed due to the depolarization effect [17]. Zaric *et al.* successfully showed that this was the case for HiPco SWNTs up to 45T [18]. Other optical experiments regarding Aharonov-Bohm physics in carbon nanotubes include magneto-photoluminescence spectroscopy on dark-excitations in SWNTs (macroscopically [19, 20, 21] and microscopically on single nanotubes[22]).

2.3 Novel Magnetic Properties of SWNTs

Ajiki and Ando then extended their interpretation of the Aharonov-Bohm effect to the magnetic properties of SWNTs [16, 23]. They found that the magnetic properties of single-walled carbon nanotubes change with the direction of the magnetic field with respect to the tube axis, yielding a magnetic anisotropy given by $\Delta\chi = |\chi_{\parallel} - \chi_{\perp}|$. Metallic nanotubes are paramagnetic along the tube axis ($\chi_{\parallel} > 0$) and diamagnetic in the perpendicular direction ($\chi_{\perp} < 0$), whereas semiconducting tubes are diamagnetic in all directions ($\chi_{\parallel} < 0$ and $\chi_{\perp} < 0$). They calculated $\Delta\chi \sim 1 - 2 \times 10^{-5}$ emu/mol for semiconducting SWNTs and $\Delta\chi \sim 5 - 10 \times 10^{-5}$ emu/mol for metallic nanotubes as seen in Fig. 2.3. Furthermore, they found that $\Delta\chi$ scales linearly with diameter.

Similarly, Lu also investigated the magnetic properties of SWNTs using a London

approximation in the same manner as theorists at that time used to studying benzene rings in C_{60} [1]. He also predicted that metallic and semiconducting nanotubes have very different magnetic susceptibility anisotropies with values on the same order as Ajiki and Ando. From Fig. 2.3 at 90° (χ_{\parallel}), both metallic and semiconducting nanotubes are diamagnetic, but as θ increases to 0° (χ_{\perp}) metallic nanotubes' χ increases to be paramagnetic. Lu calculated χ from the following equation [24]:

$$\chi = -\frac{\partial^2 F(H, T)}{\partial H^2} \quad (2.5)$$

where the Free energy, $F(H, T)$, is a function calculated from the temperature, magnetic field and the band structure. As the magnetic flux increases through the nanotube, the equation changes for metallic nanotubes such that they become paramagnetic in that direction. This is a result of the bandgap increasing as due to the Aharonov-Bohm flux through the nanotube. Similarly, for semiconducting nanotubes the bandgap decreases with magnetic field resulting in diamagnetism from Equation 2.5.

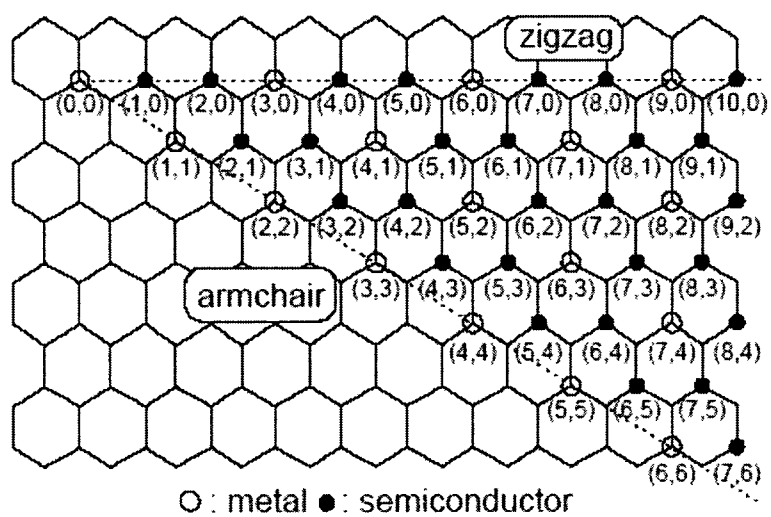


Figure 2.1 : Graphene sheet with labeled (n, m) for metallic and semiconducting SWNTs from Ref. [15].

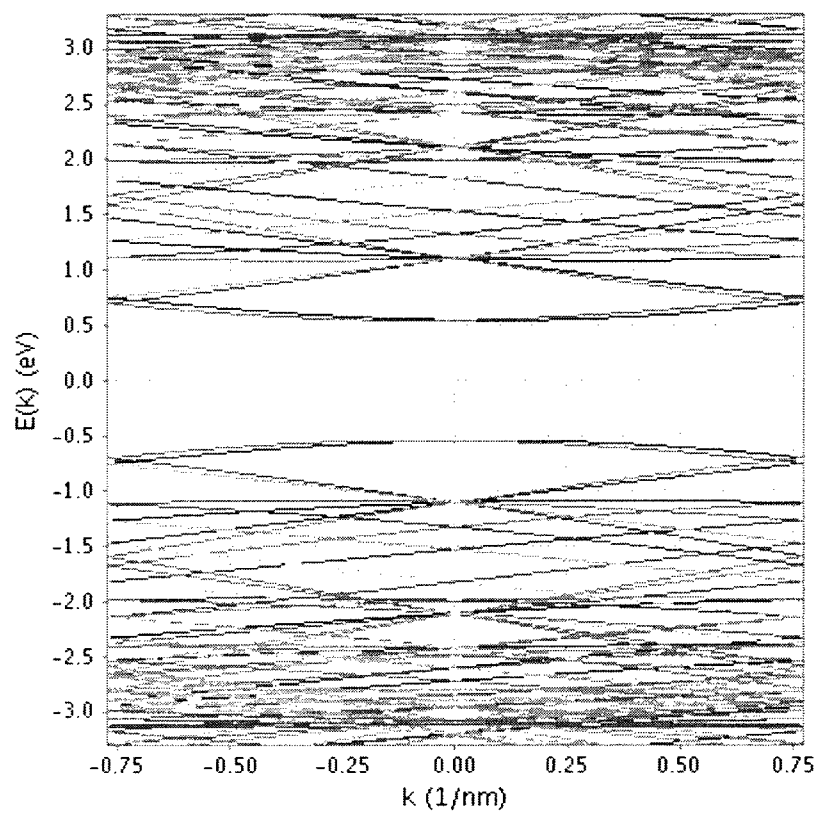


Figure 2.2 : Dispersion E vs. k for semiconducting (6,5) nanotube. (Developed through the use of the nanotube calculator (Boston University))

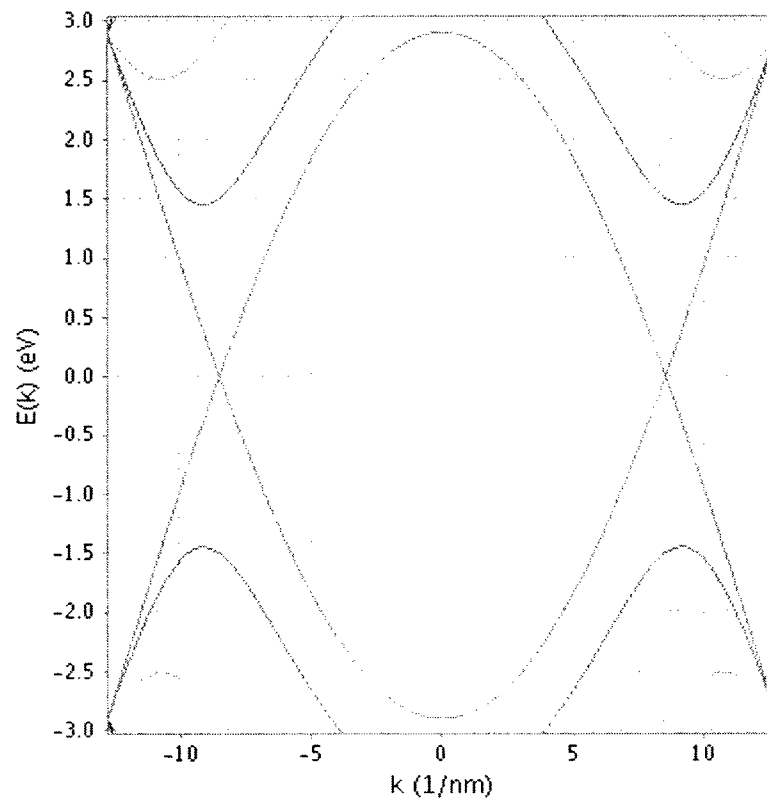


Figure 2.3 : Dispersion E vs. k for metallic (6,6) nanotube. (Developed through the use of the nanotube calculator (Boston University))

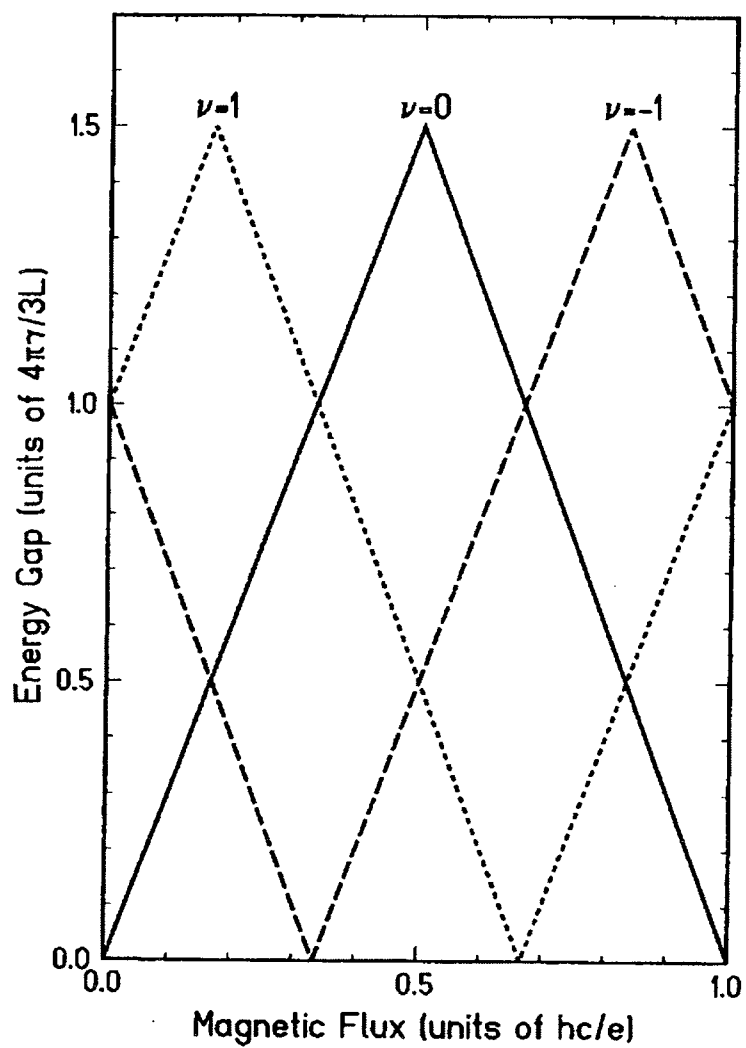


Figure 2.4 : Bandgap as a function of magnetic flux through the nanotube. Note that it oscillates for both semiconducting ($\nu = \pm 1$) and metallic ($\nu = 0$) nanotubes. (Ref. [17]))

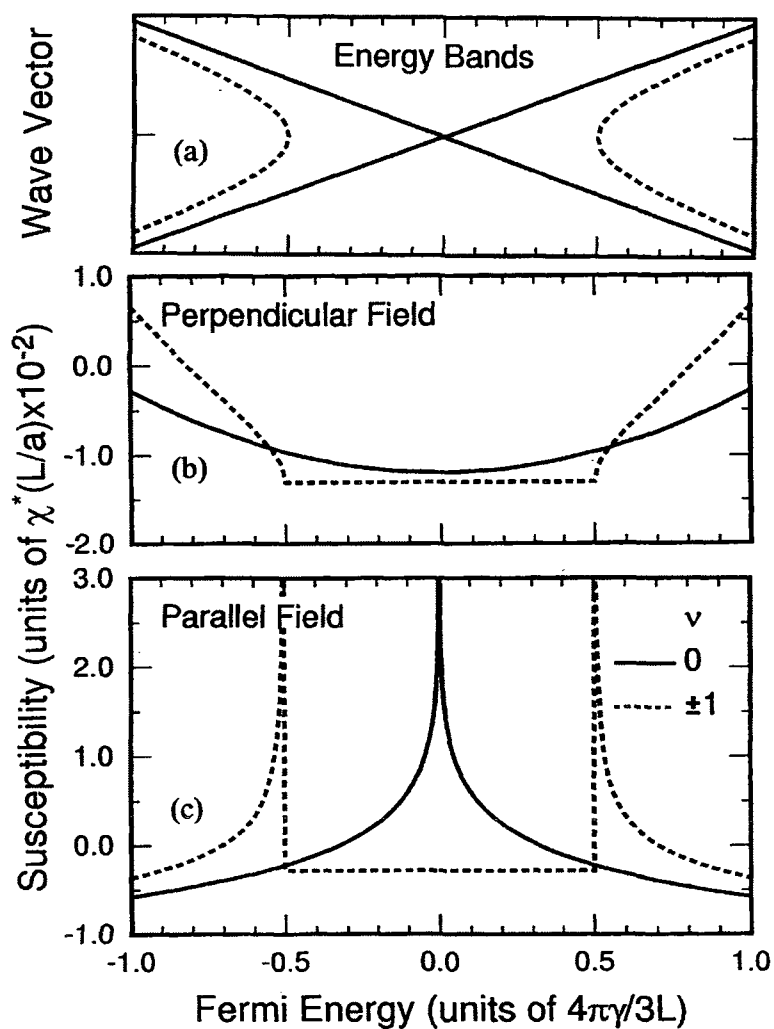


Figure 2.5 : (a) Bandgap as a function of Fermi Energy, E_f . (b) χ_{\perp} for semiconducting ($\nu = \pm 1$) and metallic nanotubes ($\nu = 0$) as a function of E_f (c) χ_{\parallel} for semiconducting and metallic nanotubes as a function of E_f (Ref. [23]).

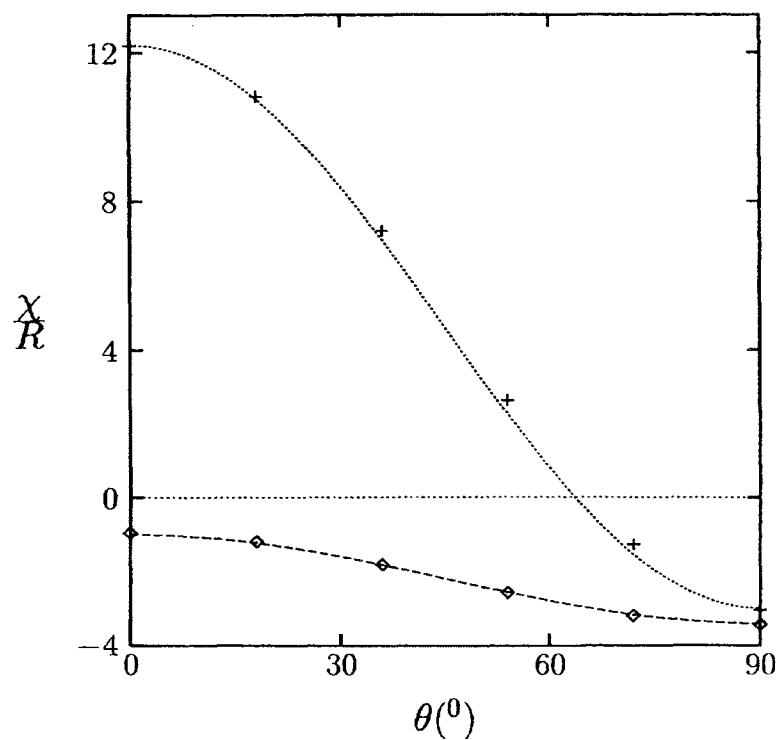


Figure 2.6 : Angular dependence of χ for SWNTs, where $\theta = 90^\circ$ is χ_\perp and $\theta = 0^\circ$ is χ_\parallel . Note that $\Delta\chi$ for metallic nanotubes (dotted) is 5 larger than $\Delta\chi$ for semiconducting nanotubes (dashed) (Ref. [24]).

Chapter 3

Previous Work on Magnetic Susceptibility Anisotropy of Semiconducting Nanotubes

3.1 Estimation of $\Delta\chi$ using Magneto-Photoluminescence

Zaric *et al.* were the first to experimentally confirm the theoretical predictions presented by Ajiki, Ando, and Lu with their measurements on HiPco nanotubes. They performed magneto-photoluminescence excitation (PLE) spectroscopy up to 45T using the hybrid magnet at the National High Magnetic Field Laboratory in Tallahassee, FL as seen in Fig. 3.1 [25]. The magnetic susceptibility anisotropy was estimated by measuring the amount of redshift in the photoluminescence (PL) spectrum and extracting values for u , a dimensionless ratio of the alignment energy and the thermal energy such that $u \equiv \sqrt{\frac{B^2 N \Delta\chi}{k_B T}}$. As a result, this parameter u is a function of N the number of carbon atoms per unit length, magnetic field B , and temperature T .

One can use the Maxwell-Boltzmann distribution function for the probability density of an ensemble of SWNTs being at an angle θ with respect to the direction of the magnetic field is given as:

$$P_u(\theta) = \frac{\exp(-u^2 \sin^2 \theta) \sin \theta}{\int_0^{\pi/2} \exp(-u^2 \sin^2 \theta) \sin \theta d\theta} \quad (3.1)$$

Using Equation 3.1 and the definition of u they found that for their sample,

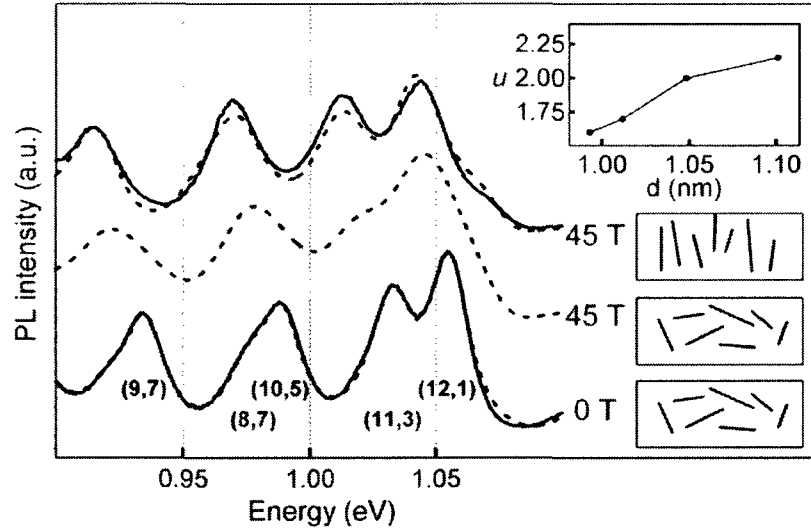


Figure 3.1 : Magneto-PL spectra of HiPco SWNTs up to 45T from Ref [25]. Note that for all chiralities present, there is a substantial redshift for each peak. The inset shows the diameter dependence of u as defined in 3.1

$\Delta\chi$ increased linearly with diameter. Furthermore, they confirmed that $\Delta\chi$ is $\sim 10^{-5}$ emu/mol for semiconducting SWNTs [16, 24, 23].

3.2 Measurement of the Polarized Optical Absorption Cross Section of SWNTs

Through the use of polarized absorption spectroscopy, the Kikkawa group at University of Pennsylvania investigated the polarized optical absorption cross section of laser oven nanotubes [26]. They suspended the nanotubes in a gel while simultaneously aligning the SWNTs with the use of a 9 T magnet. From polarized Raman spectroscopy measurements they independently determined that their nanotubes with an average length of ~ 500 nm had a $\Delta\chi = 6.7 \times 10^{-5}$ emu/mol. This large magnetic

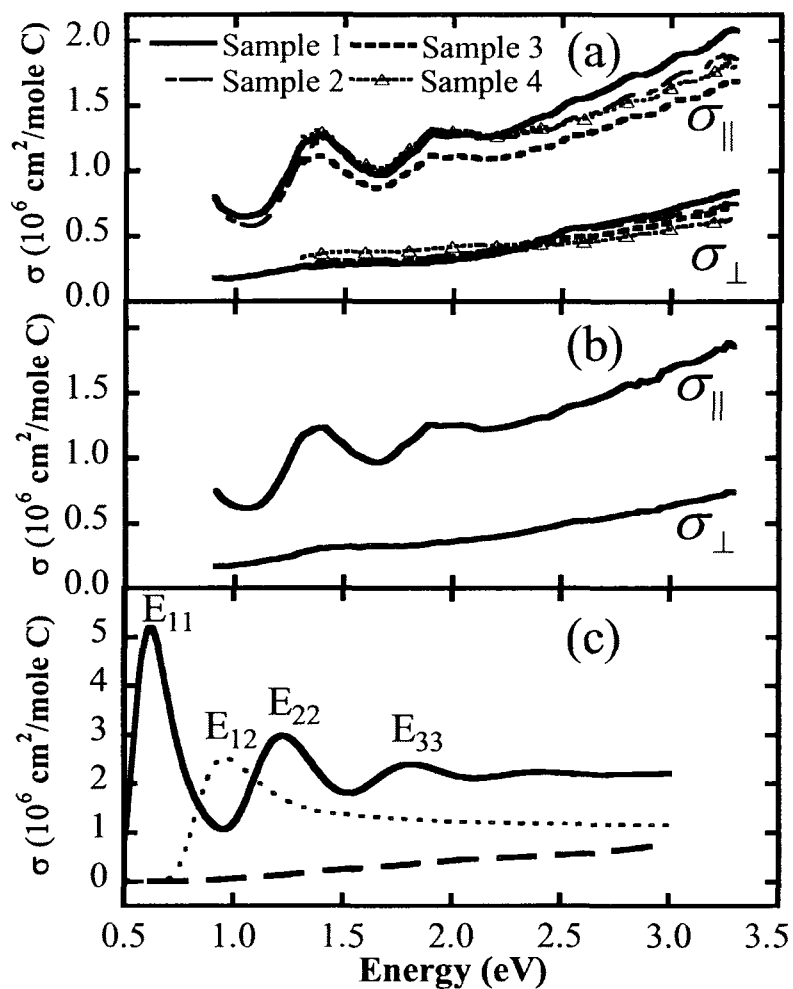


Figure 3.2 : (a) Polarized optical absorption cross section data for semiconducting laser oven SWNTs (b) Average of the spectra from the four samples (c) Modeling of spectra of (b) to show the effect of depolarization. The solid curve is for σ_{\parallel} . And the dashed line is for σ_{\perp} with depolarization effect and the dotted is σ_{\perp} without this effect. Adapted from Ref. [26].

anisotropy was attributed to the presence of ferromagnetic particles in their sample.

With this degree of alignment, they were able to extract the polarized optical absorption cross section of SWNTs which can be seen in Fig. 3.2. They averaged each of the samples seen in Fig. 3.2(a) to get the spectra seen in (b). Then they modeled σ_{\parallel} , σ_{\perp} with the effect of depolarization, and σ_{\perp} without this effect. For the latter case, it was shown by the dotted line of (c) that the cross-polarized optical transition E_{12} arises for σ_{\perp} . However, by including this effect (dashed line), they explain why they do not see this peak for their data in (b). They attribute the depolarization effect to screening from inducing charge on the surface of the nanotube [26, 17].

3.3 Influence of Ferromagnetic Particles on $\Delta\chi$

As a way to probe the reasoning behind the large $\Delta\chi$ found in their previous work (Sect.3.2), the Kikkawa group at University of Pennsylvania wanted to investigate the influence of ferromagnetic catalyst particles on the magnetic alignment of SWNTs [27]. They performed magneto-absorption spectroscopy on fractionated and unfractionated HiPco and laser oven nanotubes. To remove ferromagnetic catalysts from their fractionated samples, they utilized a magnetic gradient by passing their nanotubes through a magnetic flow chamber. Figure 3.3 shows data comparing $S(B)$ the fractionated and unfractionated for both types of SWNTs. In the absence of most of the contribution from ferromagnetic particles, they extracted $\Delta\chi$ for laser oven nanotubes to be $\Delta\chi \sim 3.2 \pm 0.8 \times 10^{-5}$ emu/mol: however no value of $\Delta\chi$ for their

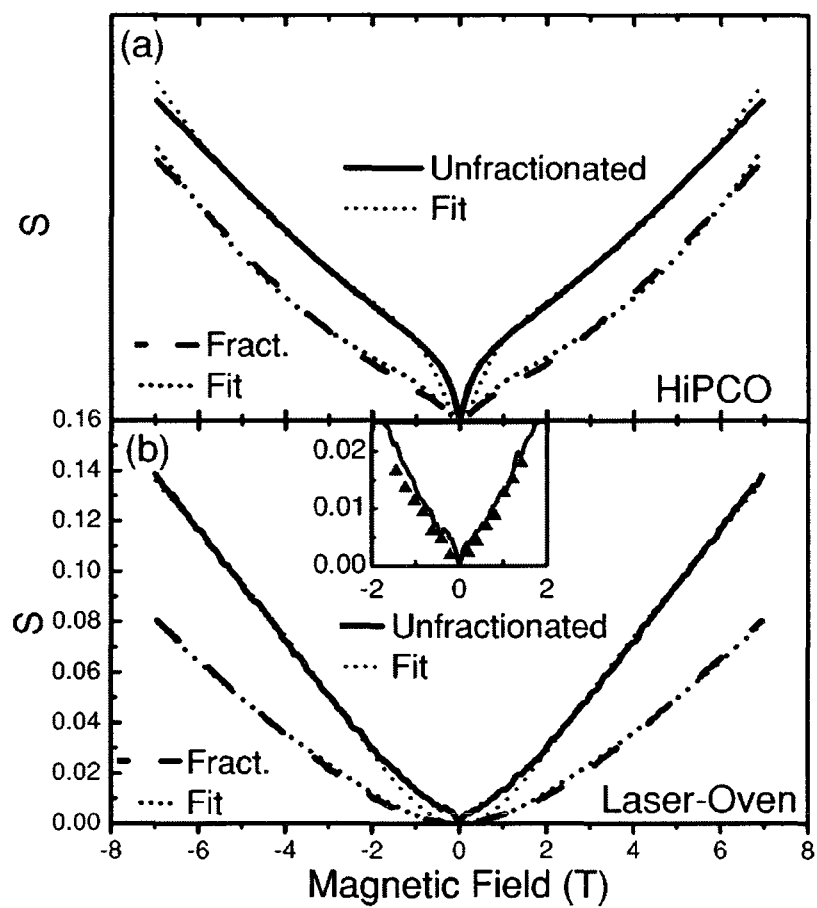


Figure 3.3 : $S(B)$ for fractionated (no contribution from ferromagnetic (FM) particles) and unfractionated (with contribution) (a) HiPCO and (b) laser oven SWNTs [27].

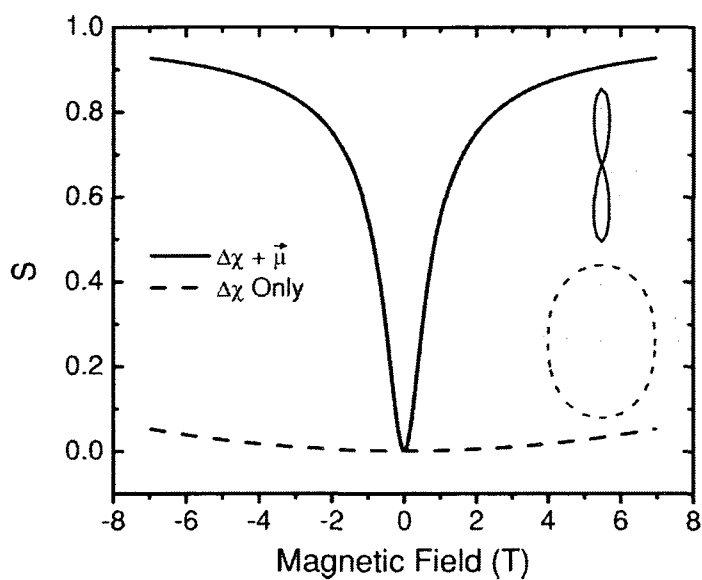


Figure 3.4 : $S(B)$ for $\vec{\mu}$ -driven (SWNTs aligning due to FM particle contribution and magnetic susceptibility anisotropy denoted by the solid line) and $\Delta\chi$ -driven (alignment is only from magnetic susceptibility anisotropy denoted by the dashed line) SWNTs. Note that the latter has a much lower alignment, whereas the former reaches complete alignment at much smaller fields [27].

HiPco sample was reported [27]. Figure 3.3 illustrates the vast difference between the influence of SWNTs whose alignment is not from $\Delta\chi$, but rather it results from $\vec{\mu}$, permanent magnet moments imposed on select SWNTs. This effect of $\vec{\mu}$ -driven SWNTs saturates at $B > 1$ T, therefore experiments about that threshold should have little contribution of these SWNTs in a large ensemble.

3.4 Chirality Dependence of $\Delta\chi$

At much lower magnetic fields than Zaric *et al.* (up to 7 T) the Kikkawa group at University of Pennsylvania, continued their work on magnetic alignment by carrying out magneto-PL measurements on DNA-wrapped CoMoCAT SWNTs. They were able to subtract out the magnetic susceptibility anisotropy of DNA [28] ($\Delta\chi \sim 0.86 \pm 0.3 \times 10^{-6}$ emu/mol) to measure four different magnetic susceptibility anisotropies for the (6,5), (7,5), (8,3) and (6,4) semiconducting nanotubes. As a result, they found that the diameter dependence predicted by Ajiki, Ando, and Lu was not valid for the nanotubes in their sample. Their values for $\Delta\chi$ follow a chiral index family dependent model as seen in Fig. 3.4. Nonetheless, they found overall agreement with previous literature that $\Delta\chi$ is $\sim 10^{-5}$ emu/mol for semiconducting nanotubes. The result that $\Delta\chi$ is not a function of diameter was later shown theoretically for zigzag semiconducting nanotubes (where $m = 0$ for (n, m) chirality) [29].

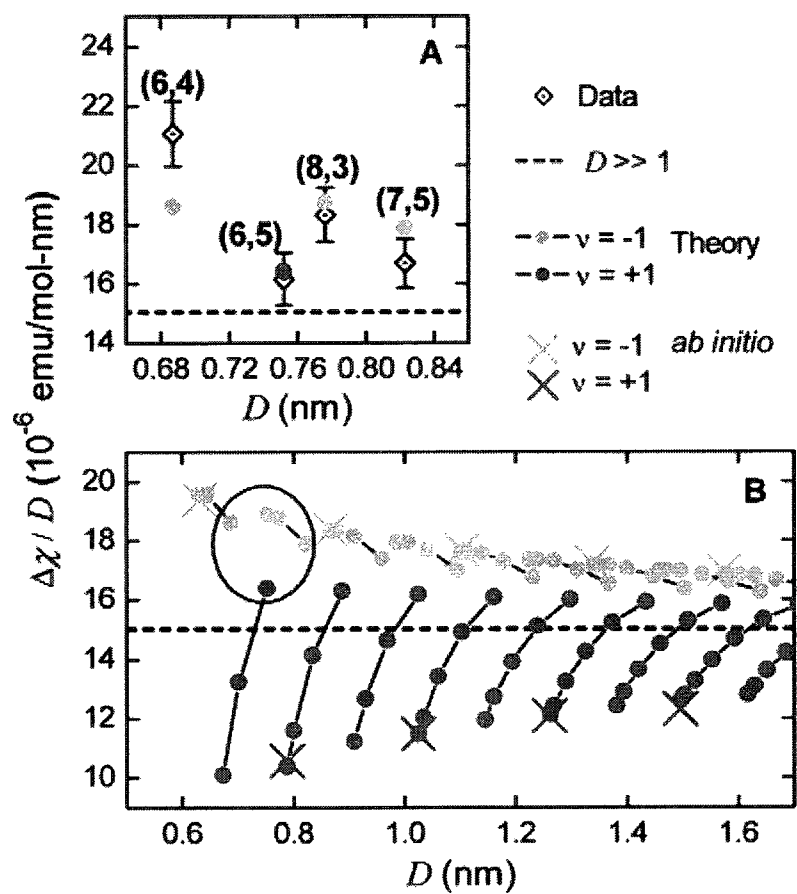


Figure 3.5 : $\Delta\chi$ as a function for diameter for semiconducting CoMoCAT nanotubes from Ref [28]. The data in (a) is fit to the family dependent theory shown in B for many nanotubes.

Chapter 4

Magnetic Susceptibility Anisotropy of Metallic SWNTs

Polarized magneto-optical absorption measurements on length-sorted, (6,5)-enriched CoMoCAT SWNTs were made using the 35 T Hybrid Magnet in the High Magnetic Field Facility of the National Institute of Materials Science in Tsukuba, Japan. We present the first experimental estimation of the magnetic susceptibility anisotropy of metallic single-walled carbon nanotubes showing their large susceptibility anisotropy. We also present a comparison of the magnetic susceptibilities of metallic and semi-conducting nanotubes within the same sample and show that the susceptibilities are $2 - 4\times$ greater in metallic nanotubes. Previous work (chapter 3) was limited to semi-conducting nanotubes because of the method of using magneto-photoluminescence to estimate the magnetic susceptibility of their respective HiPco or CoMoCAT nanotubes.

4.1 Experimental Methods

4.1.1 Sample

CoMoCAT SWNTs were suspended in 1% sodium deoxycholate and length sorted by dense liquid ultracentrifugation [30] to have an average length of $\sim 500\text{nm}$. PLE

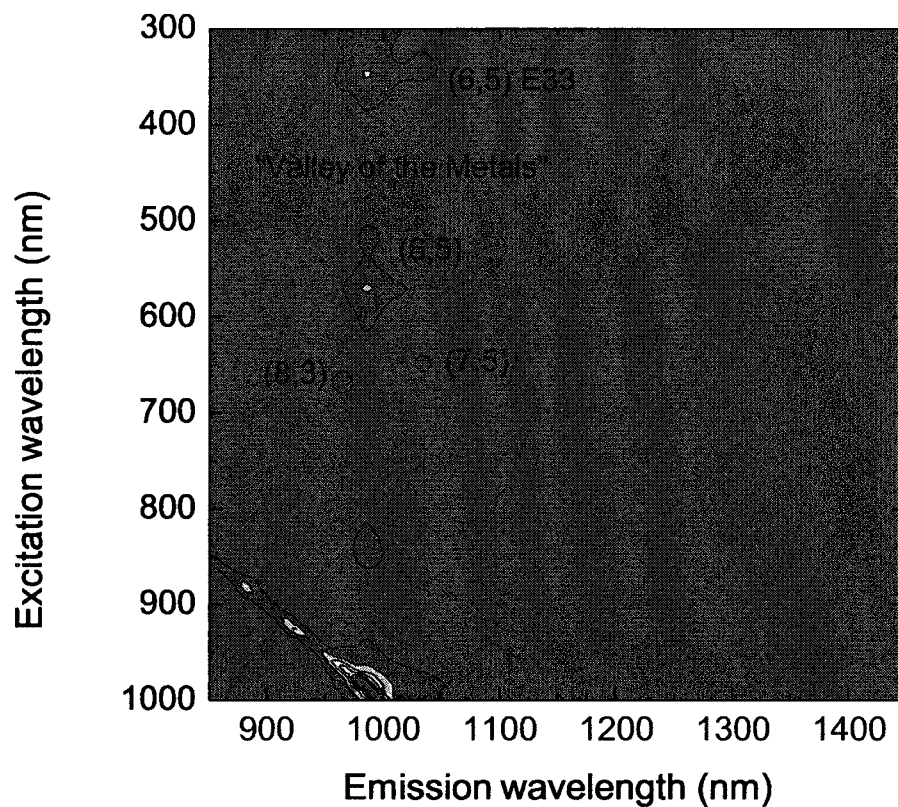


Figure 4.1 : PLE map of our NIST (6,5)-enriched length- sorted CoMoCAT sample. Note that there are only a few chiralities present. Also note that in the “Valley of the metals” there is no luminescence present.

and UV-Vis-NIR absorption spectroscopy for this CoMoCAT sample can be seen in Figs. 4.1 and 4.2, respectively. Note that the sample is well separated for a single chirality (6,5) although other chiralities are present in the PLE map. Also, note that PLE is limited to only information about semiconducting nanotubes in the sample because metallic nanotubes do not fluoresce due to the absence of a bandgap.

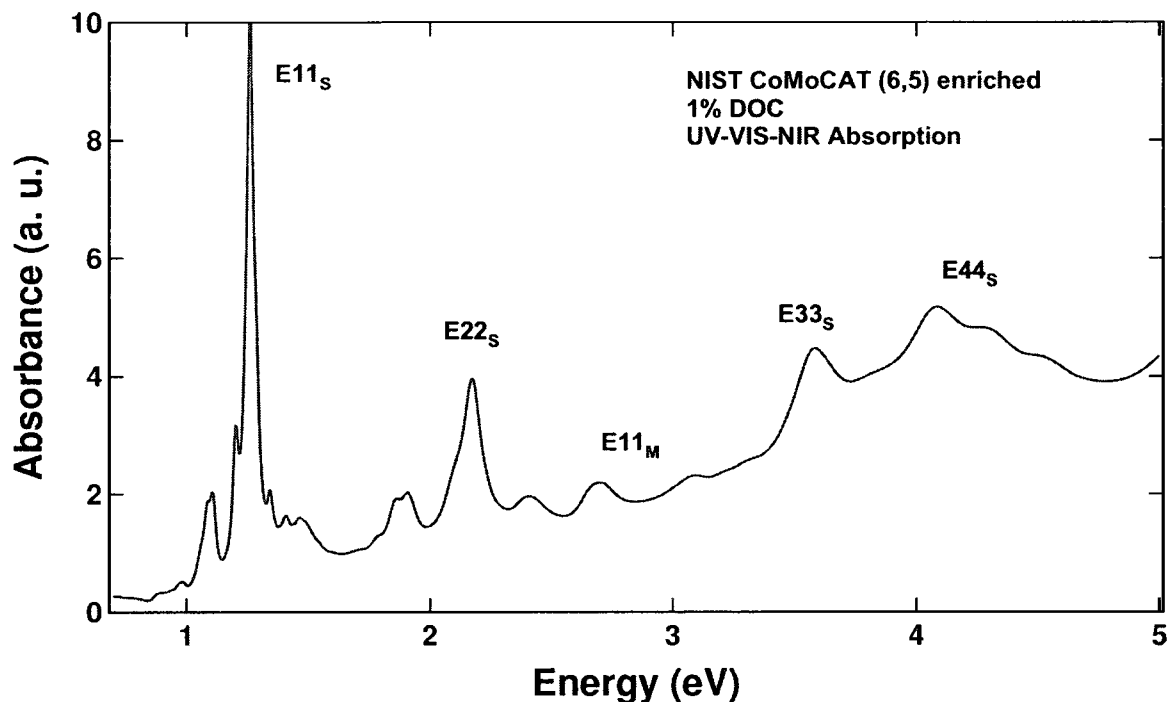


Figure 4.2 : Absorbance spectra from UV-Vis NIR Spectroscopy of our NIST (6,5)-enriched length- sorted CoMoCAT sample.

Conversely, UV-Vis-NIR absorption spectroscopy yields qualitative information about the individualization, interband transitions, and chiralities present in a given sample for both metallic and semiconducting nanotubes. In the range of 1 to 5 eV, there are five main optical transitions for SWNTs as labeled in Fig. 4.2: a) E_{11} semiconductor, b) E_{11} metallic, c) E_{22} semiconductor d) E_{33} semiconductor, and e) E_{44} semiconductor transitions. For this sample, note that there is a very high absorbance in E_{11} of (6,5) in comparison to that of E_{22} and other optical transitions of other chirality nanotubes. This was achieved by combining several long fractions from three different but similar CoMoCAT batches.

In each case, the nanotubes were dispersed with 1 h tip sonication (1/4" tip, \sim 35 mL batches, in ice bath) in 2% mass/vol sodium deoxycholate solution. The liquid was then centrifuged for 2 h at 10 °C and 18000 RPM in a JA-20 rotor, which provides roughly 38000 G max acceleration. After the two hours, the supernatant was collected and the bottoms discarded. These solutions were then concentrated against a 30 kD membrane to increase the concentration, and then length sorted via ultracentrifugation at either 12000 RPM (15 °C) or 25300 RPM (4 °C) in a SW-32 rotor for either \sim 74 h or 21 h, respectively (equivalent integrated accelerations). The length separation was done in either 2% doc, 18% mass/vol iodixanol top layers (12 k sort) or with a 2% DOC, 15% mass/vol iodixanol top layer[31]. Fractions were sequentially extracted from the top and like fractions were combined from multiple tubes/runs. For this sample, fractions from different batches of similar length were added together, and the iodixanol removed by use of a forced filtration cell (with a 30 kD membrane), with exchange into 1% DOC.

Sample preparation methods to achieve chirality and metallic separations have created a very rich field and further progress will only yield a more ideal system to study 1D physics in nanotubes and hopefully also lead to many useful applications for SWNTs. The major challenge preventing widespread technology on chirality separation is that the yields produced by methods like density gradient ultracentrifugation and other separation techniques like DNA sequencing are much lower than anything useful for applications at this time; on the order of 0.1 to 0.8 μg per 100 μg [32].

In comparison to previous work [18, 25], our sample also provided two distinct advantages for performing this experiment. First, our sample was length-sorted to yield an average length. Size exclusion chromatography is a well developed technique that has been compared with atomic force microscopy (AFM) to insure the accuracy of the lengths produced [30]. Thus, there was no need to perform additional AFM to determine the average length statistically on a sample set of nanotubes present in our solution. Furthermore, in Ref. [18] the average length was reported to be 300 nm, and therefore, the alignment from our sample should be much better because we are using longer tubes, 1 μ m. The second advantage of our sample comes from the fact that it is enriched for chirality from CoMoCAT batches. When our group tried magneto-absorption spectroscopy with HiPco [18], results and analysis were very complicated due to the many different chirality nanotubes present in that type of sample. With our sample, we are limited to a small number of nanotubes with four dominate semiconducting nanotubes [(8,3),(6,4),(7,5) and (6,5)] and three metallic nanotubes [(6,6), (7,4) and (5,5)].

4.1.2 Hybrid Magnet

The hybrid magnet at the National Institute of Material Science allows users to operate at DC fields up to 35 T[33]. The term hybrid comes from the fact that the resistive insert sits inside of the 400 mm bore of a superconducting magnet whose maximum field is 14.2 T . The resistive insert is made up of three Bitter magnet coils

(Fig. 4.3) with 10.4 T coming from the inner coil, 7.9 T from the middle coil and 5.8 T from the final outer coil.

Adding these fields together gives a total of 37.3 T only surpassed in DC fields by the 45 T Hybrid at the National High Magnetic Field Laboratory in Tallahassee, FL [34]. The sample space for this magnet is 32 mm and is held at room temperature. The magnet is placed underground as seen in Fig. 4.4.

4.1.3 Experimental Setup

A Xe lamp fiber coupled to a custom optical probe allowed for broadband white-light excitation of the E_{11} metallic, E_{22} semiconductor, and E_{33} semiconductor optical interband transitions of SWNTs. The solution sample was held in a cuvette with a film polarizer directly on the front face to allow for linear polarization of the incident light. Collimated light was collected with another fiber and dispersed through a monochromator where the spectra were measured using a Si CCD. A schematic of the sample probe can be found in Fig. 4.5, The temperature of the sample was ~ 300 K.

4.2 Experimental results

The spectra from our polarized magneto-optical absorption spectroscopy of 0 to 35 T are shown in Fig. 4.6. The data is not intentionally offset, indicating an increase in absorbance for light polarized parallel to the nanotube axis, and a decrease in

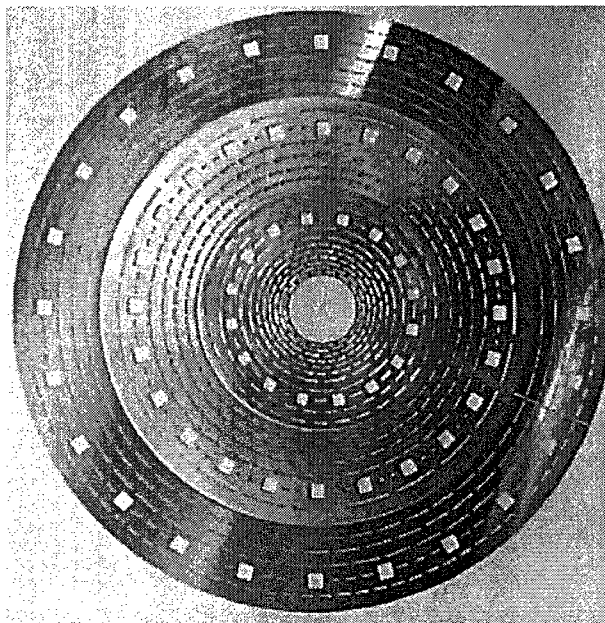


Figure 4.3 : Resistive Magnet Insert Coils of Bitter Magnet adapted from [33]

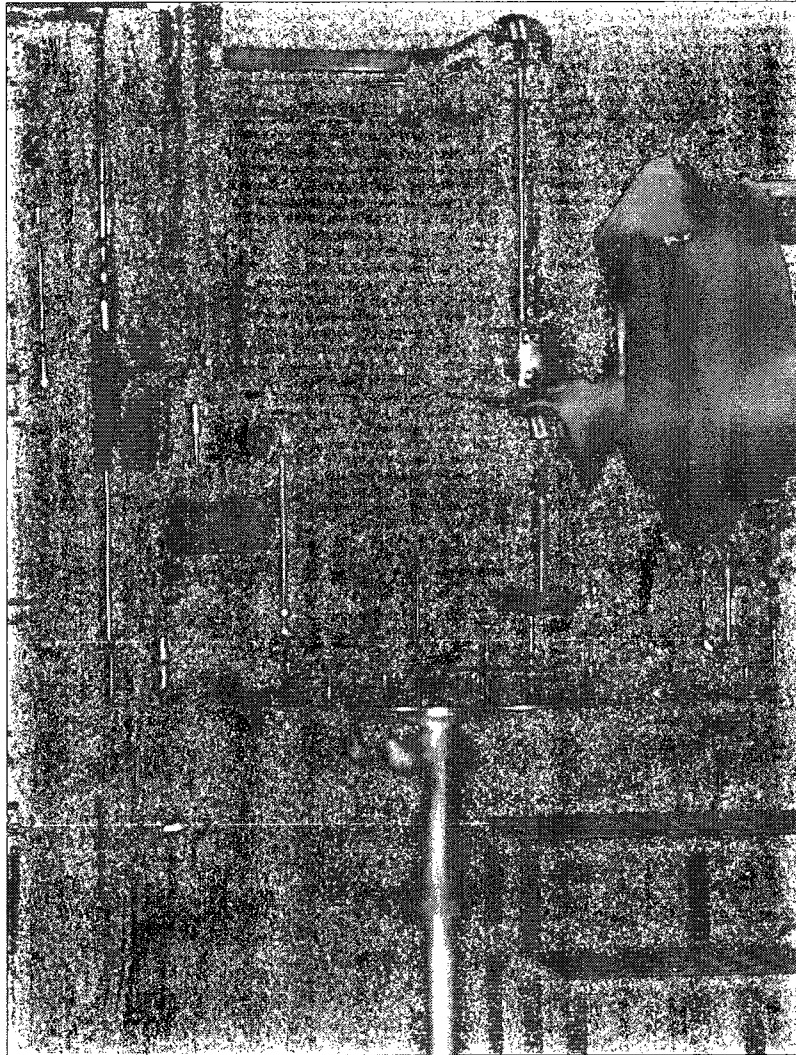


Figure 4.4 : Photograph of the NIMS Hybrid Magnet

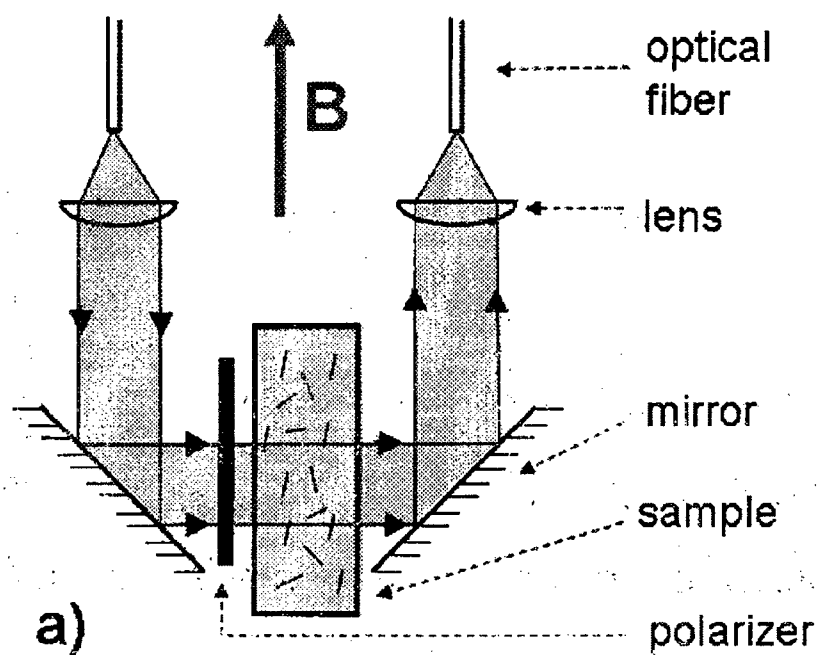


Figure 4.5 : Optical path of Polarized Magneto-optical Absorption Spectroscopy Probe [35].

absorbance for light polarized perpendicular to nanotube axis. This is due to the fact that nanotubes selectively absorb light in the direction along the nanotube axis corresponding to the amount of the alignment caused by the increase in magnetic field.

From the theory of linear dichroism for an ensemble of anisotropic molecules, the following quantity can be shown to be constant, independent of the degree of alignment:

$$A_0 \equiv \frac{A_{\parallel} + 2A_{\perp}}{3}. \quad (4.1)$$

Here, A_{\parallel} describes the absorption of light polarized parallel to the orientation axis, and A_{\perp} describes absorption of light polarized perpendicular to the orientation axis. A_0 for 35 T is also shown in Fig. 4.7 as a red dashed line. Note that it coincides with absorbance at 0 T, confirming that A_0 is indeed independent of alignment (or B). This is because at 0 T, $A_{\parallel} = A_{\perp}$. For subsequent fields ($B \neq 0$), the increase in absorbance for A_{\parallel} and the decrease of absorbance seen in A_{\perp} is such that the ratio of the two still preserves A_0 for the case of a rigid rod [36] (in our case a nanotube).

Linear dichroism (LD) is defined as the difference between the absorbance of polarized light parallel to the orientation axis and the absorbance of the polarized light perpendicular to the orientation axis. To adjust for differences in relative absorbances due to the fact that our sample is enriched for (6,5), the LD is divided by A_0 yielding the following result for reduced LD (LD^r) [36]:

$$LD = A_{\parallel} - A_{\perp} \quad (4.2)$$

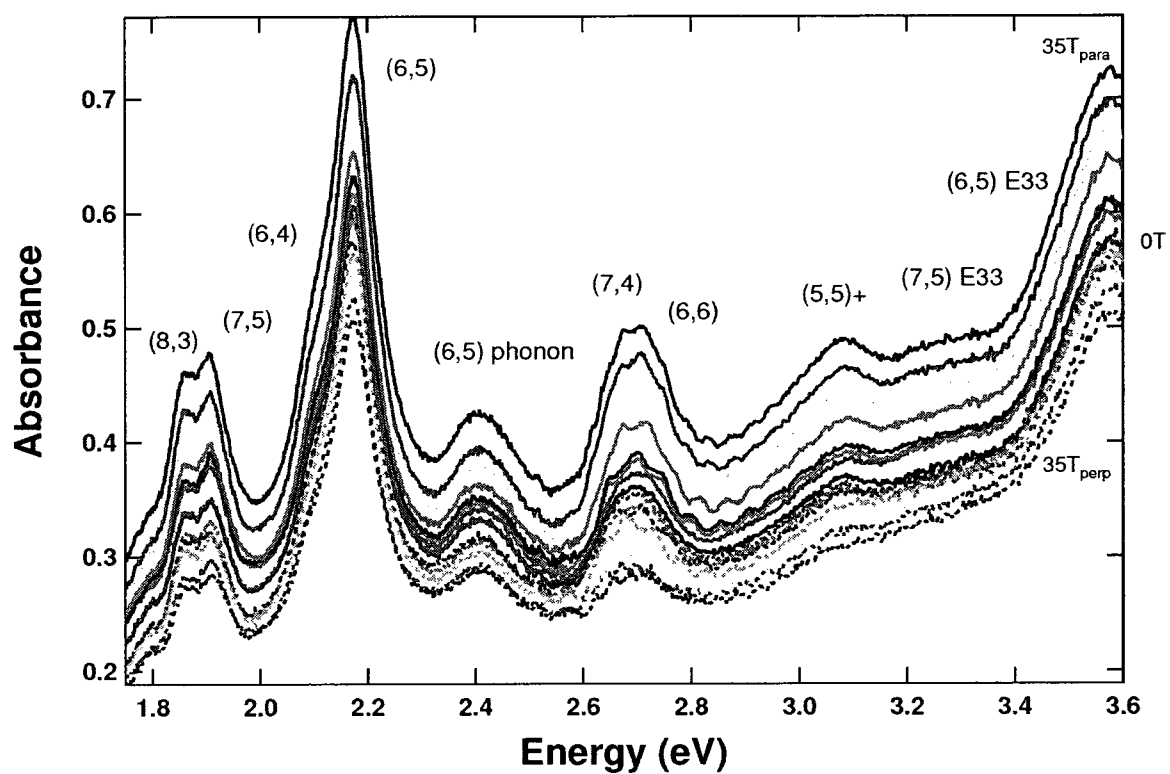


Figure 4.6 : Polarized Magneto-optical Absorption Spectroscopy from 0 to 35 T

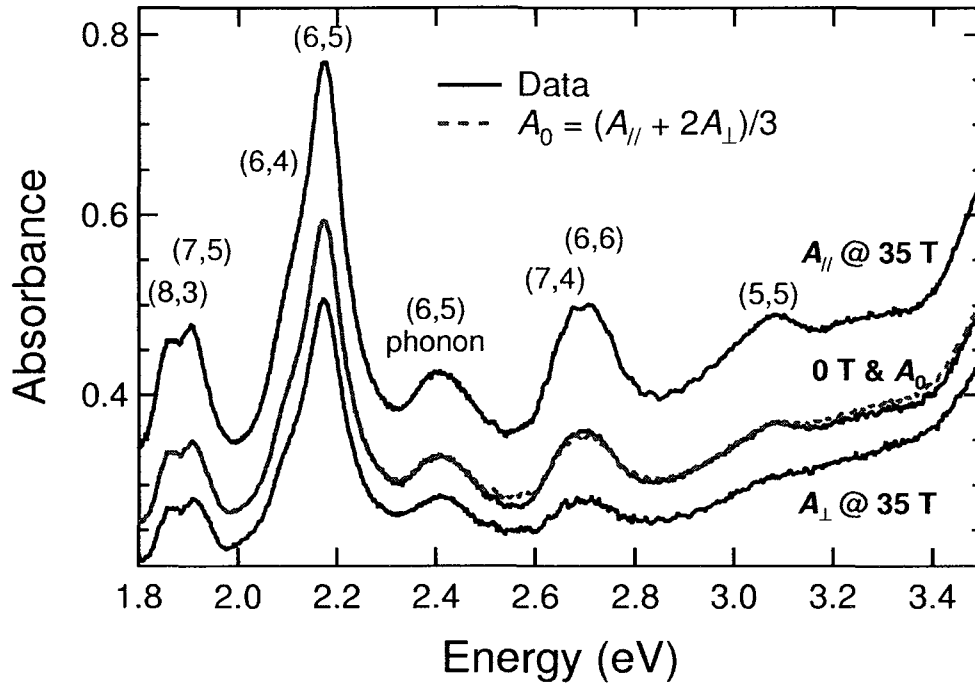


Figure 4.7 : Absorbance spectra (solid black) for 0 T and 35 T with all peaks assigned from our sample. The unpolarized isotropic absorbance (dashed red) is calculated from the magnetic field data and agrees well with that of the 0 T data.

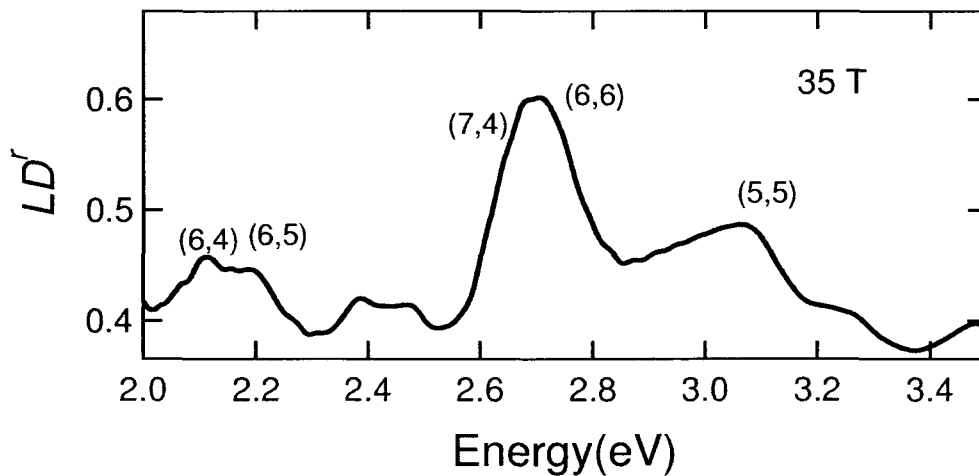


Figure 4.8 : Reduced Linear Dichroism vs Energy (eV) from measured data. The largest peak is from metallic nanotubes (6,6) and (7,4).

$$LD^r = \frac{LD}{A_0} = 3 \left(\frac{3 \cos^2 \alpha - 1}{2} \right) S \quad (4.3)$$

where S is the nematic order parameter describing the degree of alignment for an optically anisotropic rigid rod whose angle α determines the angle between the rigid rod and that of the transition moment. For our case, the absorbance of light that is measured is only from light absorbed along the tube axis. Therefore, $\alpha = 0$; and furthermore, Equation 4.2 becomes:

$$LD^r = 3 \left(\frac{3 \cos^2 \alpha - 1}{2} \right) S = 3S \quad (4.4)$$

The measured values for LD^r spectra at $B = 35$ T can be seen in Figure 4.8. Qualitatively, it is evident that the region of E_{11} metallic transitions (~ 2.5 to 3.2 eV) has the largest values for LD^r , but detailed fitting is required to extract the magnetic alignment properties of each chirality nanotube present in our sample.

4.3 Analysis

4.3.1 Fitting Methods

The results in Fig. 4.7 along with other magnetic fields up to 35 T were fit utilizing following expression:

$$A_{\text{fit}} = A_{\text{offset}} + \sum_{i=0}^N A_{\text{nanotubes}}^i \quad (4.5)$$

where $i, N \in \mathbb{Z}^+$ and each chirality nanotube in by $\Sigma A_{\text{nanotubes}}^i$ is represented as a Lorentzian. The linewidths of each Lorentzian were consistent with previous work for absorption spectroscopy in the Visible and UV [37, 38, 39]. Applying this algo-

rithm to each magnetic field, the peak centers and widths were held constant at the values determined at $B = 0$ and the amplitudes were allowed to float freely. For increasing magnetic field parallel with the polarization of the light, the amplitude of each Lorentzian is increased in the same manner as the absorbance of each spectrum. Similarly, as the magnetic field increased with light perpendicular to the tube axis, the amplitudes of the Lorentzians decreased.

Due to the proximity of our spectral range (1.75 to 3.6 eV) with UV spectral features such as the π plasmon peaks [40] and E_{44} semiconductor transitions, we added a nonlinear offset to our fitting equation also seen in Fig. 4.9 and denoted by A_{offset} . After adding each Lorentzian with offset, the fit for that field can be made with the experimental data as seen in Fig. 4.9 as a red dashed line. The physics behind this offset can be attributed to π plasmon peaks, pellets, bundles, light scattering etc. [38, 37]. Regardless of its origin, the offset shows a dependence in magnetic linear dichroism which can be seen in Fig. 4.9 by looking at the difference in each offset for 0, 35 T parallel and 35 T perpendicular.

For each magnetic field, the parallel and perpendicular spectra were fit simultaneously with the 0 T spectrum. The following constraints were imposed on the fitting equation for each Lorentzian to preserve the optical anisotropy intrinsic to each nanotube feature:

$$A_{i0} = \frac{A_{i\parallel} + 2A_{i\perp}}{3} \quad (4.6)$$

where $i = 1, 2, 3$, etc. corresponding to each Lorentzian or chirality nanotube, and

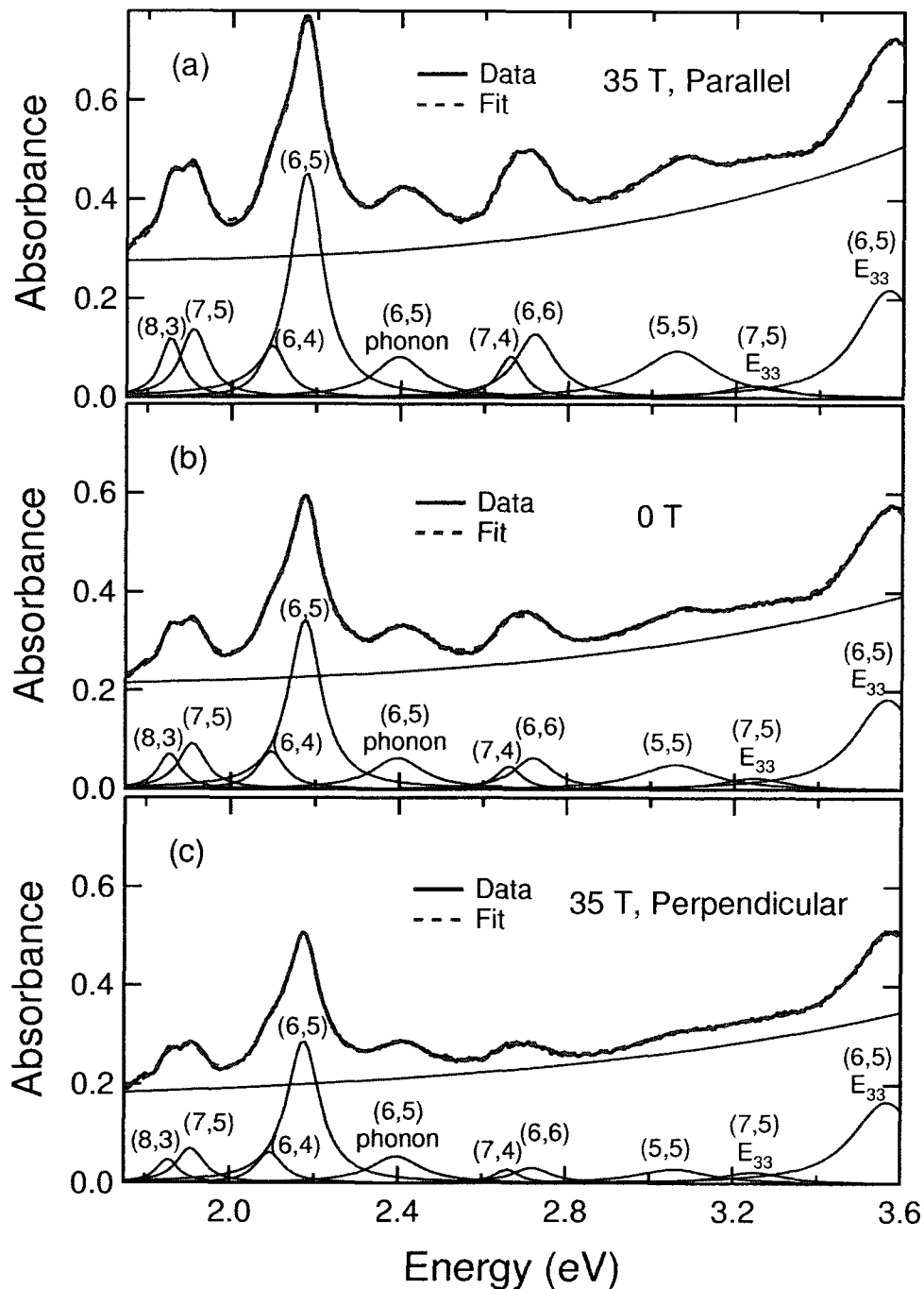


Figure 4.9 : Fitting results for 0 T and 35 T. The data (black) is fit by the sum of each individual chirality nanotube (blue) and the addition of a susceptible offset (blue). The sum of these individual fits is shown as a red line. All spectra were fit simultaneously and data for subsequent fields was performed in the same manner.

the amplitude, A . The decomposed fits for 0 T and 35 T can be seen in Fig. 4.8 with each Lorentzian assigned to a different chirality.

4.3.2 Fitting Results

Figure 4.11 shows the Lorentzians resulting from fitting for the (7,5), (6,5), (6,6), and (5,5) nanotubes at 0 and 35 T. These Lorentzians along with the others for the nanotubes present in our sample were used with Equations 4.1 and 4.2 to calculate LD and LD^r , respectively. Note that LD^r shown in Fig. 4.11 is different than that shown previously in Fig. 4.7. This is a direct result of calculating LD^r from each Lorentzian of different chirality versus calculating LD^r from the entire spectra of measured data; i.e., all of the chiralities at once. Furthermore, from our fitting procedure, LD for each chirality nanotube should just be a Lorentzian. Thus, from mathematics, we know that dividing by a Lorentzian of the same peak center and width should yield a constant value for LD^r . This is also confirmed by the fact that Equation 4.3 yields a constant value for LD^r because S by definition is constant. As a result, one can extract information on the alignment for each nanotube. It is evident that the values are much larger for the metallic than the semiconducting nanotubes suggesting that the alignment is higher at 35 T.

In the previous paragraph, it is stated that S is a constant. The nematic order parameter S is defined as the degree of alignment such that $S \equiv \frac{3\langle \cos^2 \theta \rangle - 1}{2}$ where $\langle \dots \rangle$ is the average value. For the case of a rigid rod [36], θ is the angle between

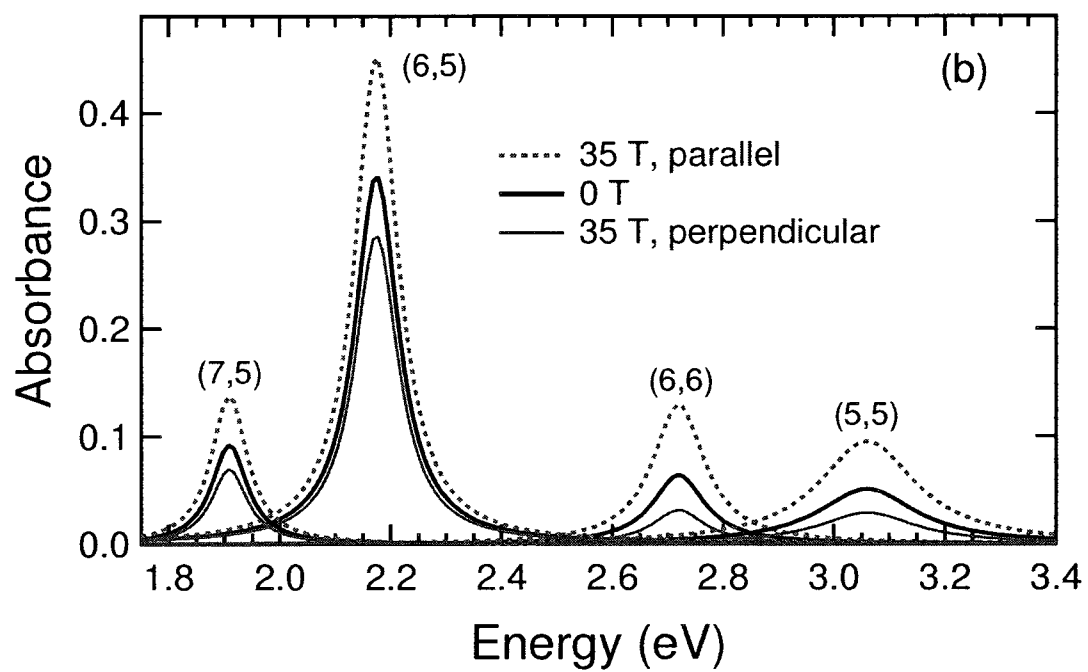


Figure 4.10 : Lorentzians for different chirality nanotubes at 0 and 35 T.

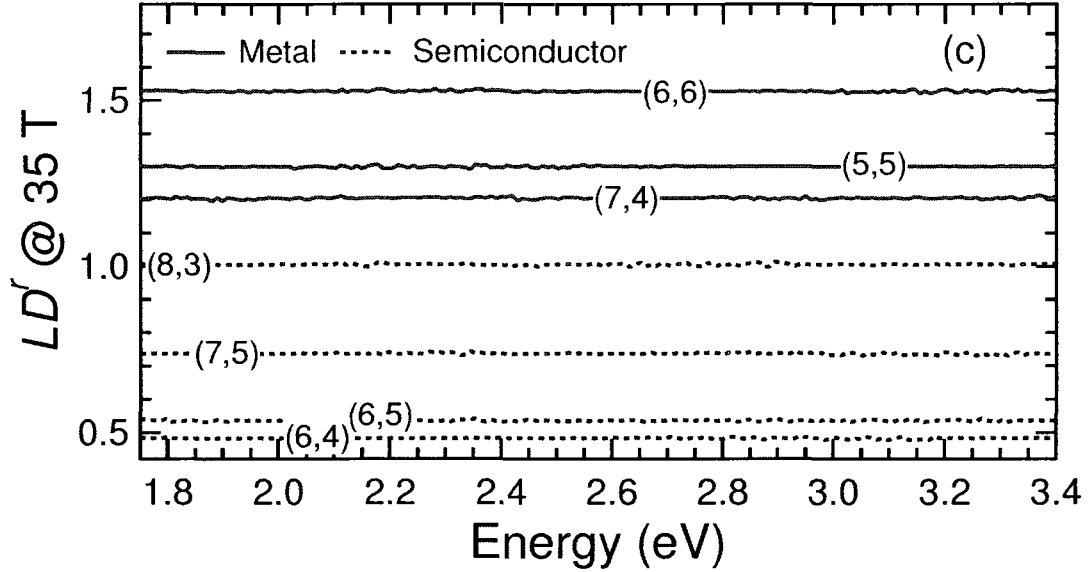


Figure 4.11 : LD^r vs. Energy (eV) derived from fitting for each individual chirality nanotube in our sample. The metallic tubes (red) are higher than the semiconducting nanotubes (blue dotted).

the magnetic field and the nanotube axis. By definition, S takes an ensemble average of the many θ given in a solution. Thus, for the case when $S = 0$, the nanotubes are completely randomized. Conversely, when $S = 1$, all nanotubes in the solution are completely aligned upright with the axis.

This allows us to use the relation $S = LD^r/3$ to calculate measured S from LD^r of each nanotube as seen in Fig. 4.11 and extract a measure of alignment. Due to the fact that our measurements were at $B > 1$ T, the effect of ferromagnetic material present in our sample will be saturated and did not effect our measured values for S or $\Delta\chi$ [27]. S as a function of magnetic field is plotted in Fig. 4.12 with the largest alignment seen from both armchair nanotubes ($n = m$ for (n, m) chirality nanotube).

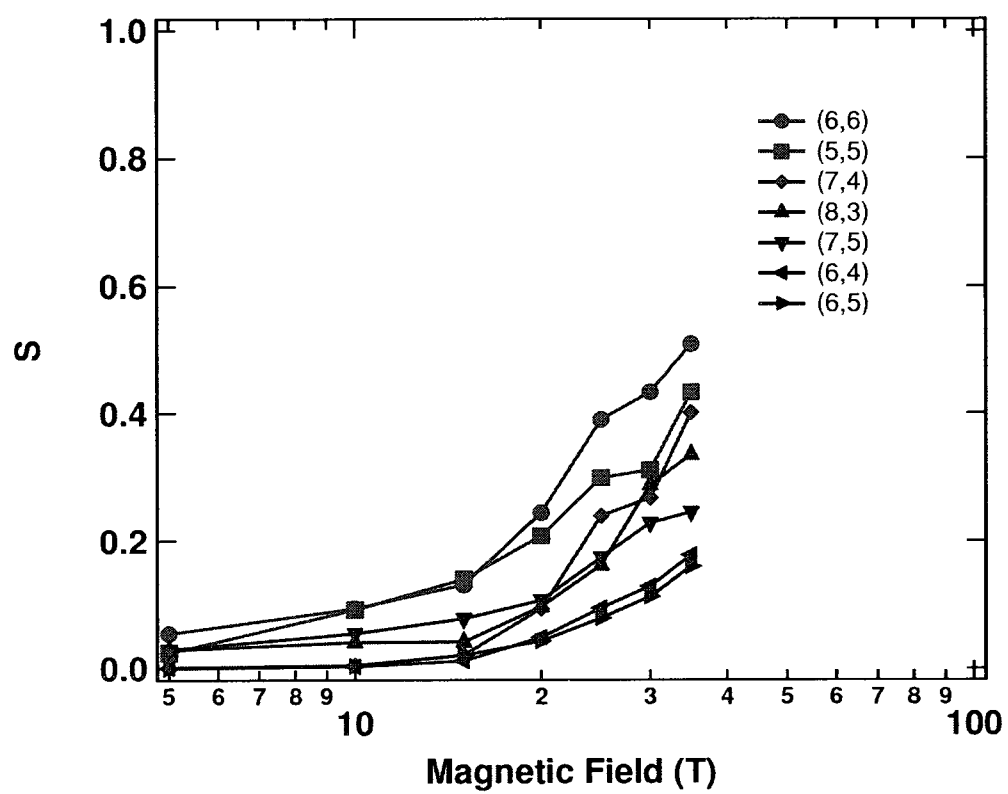


Figure 4.12 : S vs B

4.4 Discussion

The probability of an ensemble of nanotubes to align with angle θ between the nanotube axis and B can be approximated by the Maxwell-Boltzmann distribution [25]:

$$P_u(\theta) = \frac{\exp(-u^2 \sin^2 \theta) \sin \theta}{\int_0^{\pi/2} \exp(-u^2 \sin^2 \theta) \sin \theta d\theta} \quad (4.7)$$

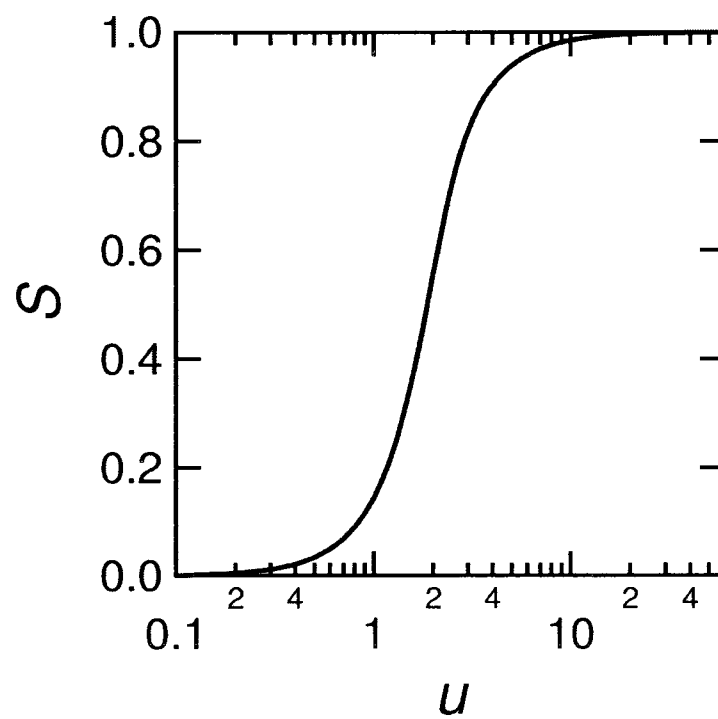
where $u = \sqrt{\frac{B^2 N \Delta\chi}{2k_B T}}$ is a dimensionless measure of the relative importance of the magnetic alignment energy ($B^2 N \Delta\chi$) and the thermal energy ($k_B T$). Here N is the number of carbon atoms per average length of the nanotubes in our sample ($1 \mu\text{m}$), k_B represents Boltzmann's constant, and T is the temperature.

For the specific case of an ensemble of nanotubes aligning with magnetic field in solution with probability $P_u(\theta)$, we can derive the following by making use of Dawson's function [41]:

$$S(u) = \frac{-1}{2} + \left(\frac{3}{4u^2} \right) \left(\frac{u}{\frac{\sqrt{\pi}}{2} e^{-u^2} \operatorname{erfi}(u)} - 1 \right) \quad (4.8)$$

where erfi is the imaginary error function ($\operatorname{erfi}(u) = \frac{2}{i\sqrt{\pi}} \int_0^{iz} e^{-t^2} dt$).

Using this equation for $S(u)$ as plotted in Fig. 4.13, we were able to extract $\Delta\chi$ for each nanotube as seen in Table 4.1. The values for the three metallic nanotubes, (7,4), (5,5), and (6,6), are all higher than those for the semiconducting nanotubes. Furthermore, it is evident that the magnetic susceptibility anisotropy of the metallic nanotubes here are consistent with the prediction [24, 23] in that metallic nanotubes have $\Delta\chi \sim 2 - 6\times$ larger than those in semiconducting nanotubes, depending on the diameter. This large difference in magnetic susceptibility anisotropy is a direct

Figure 4.13 : Model of S vs. u

consequence of the Aharonov-Bohm physics causing the band structure to change in the form of the bandgap opening in metallic nanotubes and the bandgap shrinking for semiconducting nanotubes.

Specifically for metallic nanotubes, this causes a large paramagnetism in the direction along the tube axis. This additional attraction towards the magnetic field manifests itself in the form of higher $\Delta\chi$. Figure 4.14 shows a direct comparison of the alignment with magnetic field for (6,6) and (6,5). Theoretically, larger anisotropy results in more alignment at lower fields, and higher at the same field and both of these attributes are shown in this graph.

The values for metallic nanotubes in Table 4.1 do not follow a strict diameter dependence which is predicted for zigzag semiconducting nanotubes [29] and shown experimentally in chiral semiconducting nanotubes [28]. It is also important to note that the chiral metallic nanotube, (7,4), has a value for $\Delta\chi$ lower than those found in armchairs of this study. A detailed study on a metallic enriched sample should yield many more metallic nanotubes to investigate this result (comparing metallic, zigzag, and chiral metallic nanotubes) in the future. Nonetheless, this work shows experimentally that for SWNTs $\Delta\chi$ is from 2-4 \times larger (depending on the chirality) in metallic nanotubes in comparison to semiconducting nanotubes.

When evaluating $\Delta\chi$ for the semiconducting nanotubes in Table 4.1, it is interesting to note that our values for $\Delta\chi$ are in agreement with values previously reported [18, 25, 27, 28]. $\Delta\chi$ extracted for (6,5) and (6,4) are similar to theoretic-

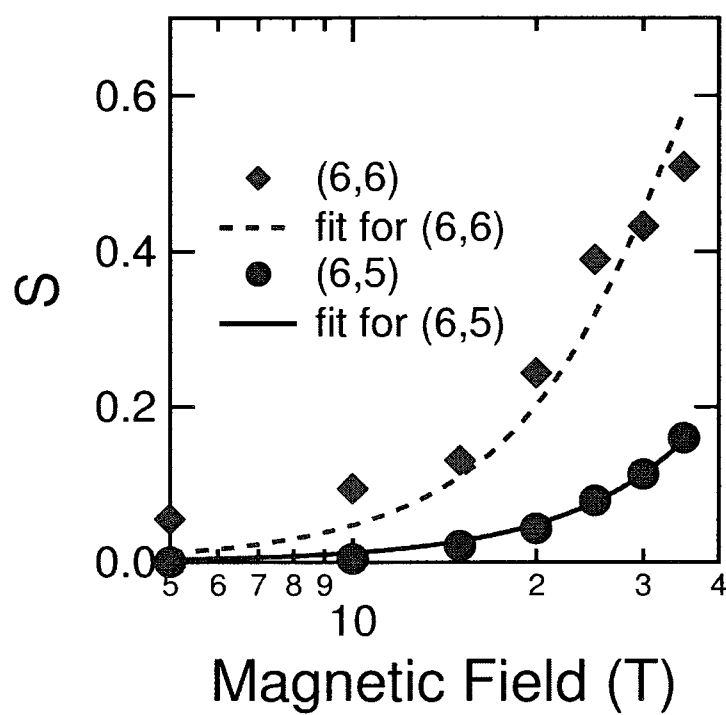


Figure 4.14 : S vs. B of (6,6) vs. (6,5)

Table 4.1 : Comparison of values of magnetic susceptibility anisotropy from previous theoretical and experimental studies and this work. For each chirality nanotube (n,m), the diameter d and the chiral index ν is given followed by estimated theoretical and experimental values of $\Delta\chi$. All values for $\Delta\chi$ are $\sim 10^{-5}$ emu/mol with the first two columns of $\Delta\chi_{th}$ corresponding to theoretical predictions for 30K and 300K respectively. For the last two columns, $\Delta\chi_{exp}$ are measured values for $\Delta\chi$ with the last column for the present work.

(n, m)	d (nm)	ν	$\alpha(^{\circ})$	$\Delta\chi_{th}^*$	$\Delta\chi_{th}^{\dagger}$	$\Delta\chi_{exp}^{\ddagger}$	$\Delta\chi_{exp}$
(6,6)	0.81	0	30	6.38	3.92	—	3.63
(5,5)	0.67	0	30	5.32	3.39	—	3.35
(7,4)	0.75	0	21	5.92	3.70	—	2.44
(8,3)	0.77	-1	15	1.48	1.46	1.4	2.13
(7,5)	0.81	-1	24	1.57	1.55	1.4	1.66
(6,5)	0.74	1	27	1.44	1.42	1.2	1.01
(6,4)	0.68	-1	23	1.31	1.29	1.4	1.24

cal predictions for those chiralities. Our values for (8,3) and (7,5) are higher than those predicted [16, 24, 23, 29] and found experimentally by [18, 25, 28], but are in close agreement to the $\Delta\chi \sim 3.2 \pm 0.8 \times 10^{-5}$ emu/mol reported for laser oven nanotubes [27]. Also as in previous studies [29, 28], our work does not follow a strict diameter dependence yielding further experimental evidence that $\Delta\chi$ is not just a function of diameter, but the chiral angle and the family dependence of chiral index ν are important factors.

4.5 Conclusion

In conclusion, we have successfully presented $\Delta\chi$ for metallic single-walled carbon nanotubes and confirmed that they are much larger than those of semiconducting nanotubes as predicted. We also compared magnetic susceptibilities of semiconducting and metallic nanotubes of the same sample experimentally. Lastly, we were able to confirm previous experimental results for the chirality dependence of the magnetic susceptibility anisotropy in semiconducting nanotubes and found that this is also true for metallic nanotubes.

Bibliography

- [1] R. C. Haddon, "Magnetism of the carbon allotropes," *Nature*, vol. 378, pp. 249–255, 1995.
- [2] W. Beaty. "Part 1: Maglev toy: diamagnetic pyrolytic carbon lifts magnet". Online video clip. YouTube. Accessed on 15 August 2009. <http://www.youtube.com/watch?v=jOaBnJpIRzM>., October 2006.
- [3] "floating pencil - diamagnetic levitation". 21 August 2008. Online video clip. YouTube. Accessed on 15 August 2009. <http://www.youtube.com/watch?v=raT13OFAqZc>, 2008.
- [4] C. Kittel, *Intro to Solid State Physics*. Wiley Scientific, 8th ed., 2005.
- [5] A. K. Geim and K. S. Novoselov, "The rise of graphene," *Nature Materials*, vol. 6, pp. 183–191, 2007.
- [6] J. W. S. Hummers and R. E. Offeman, "Preparation of Graphitic Oxide," *J. Am. Chem. Soc.*, vol. 80, no. 6, pp. 1339–1339, 1958.
- [7] K. Wakabayashi, M. Fujita, H. Ajiki, and M. Sigrist, "Electronic and magnetic properties of nanographite ribbons," *Phys. Rev. B*, vol. 59, no. 12, pp. 8271–8282, 1999.

- [8] H. W. Kroto, J. R. Heath, S. C. O'Brien, R. F. Curl, and R. E. Smalley, "C60: Buckminsterfullerene," *Nature*, vol. 318, pp. 162–163, 1985.
- [9] S. Iijima and T. Ichihashi, "Single-shell carbon nanotubes of 1-nm diameter," *Nature*, vol. 363, pp. 603–605, 1993.
- [10] D. S. Bethune, C. H. Kiang, M. S. deVries, G. Gorman, R. Savoy, J. Vazquez, and R. Beyers, "Cobalt-catalysed growth of carbon nanotubes with single-atomic-layer walls," *Nature*, vol. 363, pp. 605–607, 1993.
- [11] A. P. Ramirez, R. C. Haddon, O. Zhou, R. M. Fleming, J. Zhang, S. M. McClure, and R. E. Smalley, "Magnetic Susceptibility of Molecular Carbon: Nanotubes and Fullerite," *Science*, vol. 265, pp. 84–86, 1994.
- [12] R. S. Ruoff, D. Beach, J. Cuomo, T. McGuire, R. L. Whetten, and F. Diederich, "Confirmation of a Vanishingly Small Ring-Current Magnetic Susceptibility of Icosahedral C60," *J. Phys. Chem.*, vol. 95, no. 9, pp. 3457–3459, 1991.
- [13] Y. Aharonov and D. Bohm, "Significance of Electromagnetic Potentials in the Quantum Theory," *Phys. Rev.*, vol. 115, p. 485, 1959.
- [14] Y. Aharonov and D. Bohm, "Further Considerations on Electromagnetic Potentials in the Quantum Theory," *Phys. Rev.*, vol. 123, p. 1511, 1961.
- [15] M. S. Dresselhaus, G. Dresselhaus, and P. Avouris, eds., *Carbon Nanotubes: Synthesis, Structure, Properties, and Applications*. Springer, 2001.

- [16] H. Ajiki and T. Ando, “Magnetic properties of carbon nanotubes,” *J. Phys. Soc. Jpn.*, vol. 62, pp. 2470 – 2480, 1993.
- [17] H. Ajiki and T. Ando, “Aharonov-Bohm effect in carbon nanotubes,” *Physica B*, vol. 201, pp. 349–352, 1994.
- [18] S. Zaric, G. N. Ostojic, J. Kono, J. Shaver, V. C. Moore, M. S. Strano, R. H. Hauge, R. E. Smalley, and X. Wei, “Optical Signatures of the Aharonov-Bohm Phase in Single-Walled Carbon Nanotubes,” *Science*, vol. 304, pp. 1129–1131, 2004.
- [19] J. Shaver, S. A. Crooker, J. A. Fagan, E. K. Hobbie, N. Ubrig, O. Portugall, V. Perebeinos, P. Avouris, and J. Kono, “Magneto-optical spectroscopy of highly aligned carbon nanotubes,” *Phys. Rev. B*, vol. 78, p. 081402(R), 2008.
- [20] J. Shaver, J. Kono, O. Portugall, V. Krstic, G. L. Rikken, Y. Miyauchi, S. Maruyama, and V. Perebeinos, “Magnetic Brightening of Carbon Nanotubes Photoluminescence through Symmetry Breaking,” *Nano Lett.*, vol. 7, no. 7, pp. 1851– 1855, 2007.
- [21] I. B. Mortimer, L. J. Li, R. A. Taylor, G. L. Rikken, O. Portugall, and R. J. Nicholas. “Magneto-optical studies of single-wall carbon nanotubes,” *Phys. Rev. B*, vol. 76, pp. 085404–1 – 085404–9, 2007.
- [22] A. Srivastava, H. Htoon, V. I. Klimov, and J. Kono. “Direct Observation of

- Dark Excitons in Individual Carbon Nanotubes: Inhomogeneity in the Exchange Splitting,” *Phys. Rev. Lett.*, vol. 101, pp. 087402–1 – 087402–4, 2008.
- [23] H. Ajiki and T. Ando, “Magnetic properties of ensembles of carbon nanotubes,” *J. Phys. Soc. Jpn.*, vol. 64, p. 4382, 1995.
- [24] J. P. Lu, “Novel magnetic properties of carbon nanotubes,” *Phys. Rev. Lett.*, vol. 74, pp. 1123–1126, 1995.
- [25] S. Zaric, G. N. Ostojic, J. Kono, J. Shaver, V. C. Moore, R. E. Smalley, R. H. Hauge, and X. Wei, “Estimation of Magnetic Susceptibility Anisotropy of Carbon Nanotubes Using Magneto-Photoluminescence,” *Nano Lett.*, vol. 4, pp. 2219–2221, 2004.
- [26] M. F. Islam, D. E. Milkie, C. L. Kane, A. G. Yodh, and J. M. Kikkawa, “Direct Measurement of the Polarized Optical Absorption Cross Section of Single-Wall Carbon Nanotubes,” *Phys. Rev. Lett.*, vol. 93, no. 3, pp. 037404–1 to 037404–4, 2004.
- [27] M. F. Islam, D. E. Milkie, O. N. Torrens, A. G. Yodh, and J. M. Kikkawa, “Magnetic heterogeneity and alignment of single wall carbon nanotubes,” *Phys. Rev. B*, vol. 71, p. 201401(R), 2005.
- [28] O. N. Torrens, D. E. Milkie, H. Y. Ban, M. Zheng, G. B. Onoa, T. D. Gierke, and J. M. Kikkawa. “Measurement of chiral-dependent magnetic anisotropy in carbon nanotubes,” *J. Am. Chem. Soc.*, vol. 129, no. 2, pp. 252–253, 2007.

- [29] M. A. L. Marques, M. d’Avezac, and F. Mauri, “Magnetic response and NMR spectra of carbon nanotubes from ab initio calculations,” *Phys. Rev. B*, vol. 73, p. 125433, 2006.
- [30] X. Huang, R. S. Mclean, and M. Zheng, “High-resolution length sorting and purification of dna-wrapped carbon nanotubes by size-exclusion chromatography,” *Anal. Chem.*, vol. 77, pp. 6225–6228, 2005.
- [31] J. A. Fagan, M. L. Becker, J. Chun, P. Nie, B. J. Bauer, J. R. Simpson, A. Hight-Walker, and E. K. Hobbie, “Centrifugal Length Separation of Carbon Nanotubes,” *Langmuir*, vol. 24, pp. 13880–13889, 2008.
- [32] X. Tu, S. Manohar, A. Jagota, and M. Zheng, “DNA sequence motifs for structure-specific recognition and separation of carbon nanotubes,” *Nature*, vol. 460, pp. 250–253, 2009.
- [33] T. Asano, K. Koyanagi, S. Matsumoto, T. Kiyoshi, M. Kosuge, M. Yuyama, A. Sato, H. Wada, M. Hoshino, and Y. Dozono, “Resistive insert magnet for a 37.3T hybrid magnet,” *Physica B*, vol. 294-295, pp. 635–638, 2001.
- [34] B. L. Brandt, S. Hannahs, H. J. Schneider-Muntau, G. Boebinger, and N. S. Sullivan, “The national high magnetic field laboratory,” *Physica B*, vol. 294-295, pp. 505–511, 2001.
- [35] S. Zaric, *Optical Spectroscopy of Single-Walled Carbon Nanotubes in High Magnetic Fields*. PhD thesis, Rice University, 2007.

- [36] A. Rodger and B. Norden, *Circular Dichroism and Linear Dichroism*. Oxford: Oxford University Press, 1997.
- [37] N. Nair, M. L. Usrey, W. Kim, R. D. Braatz, and M. S. Strano, "Estimation of the (n,m) Concentration Distribution of Single-Walled Carbon Nanotubes from photoabsorption spectra," *Anal. Chem.*, vol. 78, pp. 7689–7696, 2006.
- [38] J. A. Fagan, V. Bajpai, B. J. Bauer, and E. K. Hobbie, "Anisotropic polarizability of isolated semiconducting single-wall carbon nanotubes in alternating electric fields," *Appl. Phys. Lett.*, vol. 91, p. 213105, 2007.
- [39] T. Hertel, V. Perebeinos, J. Crochet, K. Arnold, M. Kappes, and P. Avouris, "Intersubband decay of 1-d exciton resonances in carbon nanotubes," *Nano Lett.*, vol. 8, no. 1, pp. 87–91, 2008.
- [40] Y. Murakami, E. Einarsson, T. Edamura, and S. Maruyama, "Polarization dependence of the optical absorption of single-walled carbon nanotubes," *Phys. Rev. Lett.*, vol. 94, p. 087402, 2005.
- [41] J. P. Boyd, "Evaluating of Dawson's Integral by solving its differential equation using orthogonal ration Chebyshev functions," *Applied Mathematics and Computation*, vol. 204, pp. 914–919, 2008.